Structure-based mechanism of RyR channel operation by calcium and magnesium ions

Alexandra Zahradníková[1]✉, Jana Pavelková[1], Miroslav Sabo[2], Sefer Baday[3], and Ivan Zahradník[1]✉

[1] Department of Cellular Cardiology, Institute of Experimental Endocrinology, Biomedical Research Center, Slovak Academy of Sciences, Bratislava, Slovakia. [2] Bioinformatics Laboratory, Biomedical Research Center, Slovak Academy of Sciences, Bratislava, Slovakia. [3] Applied Informatics Department, Informatics Institute, Istanbul Technical University, Istanbul, Türkiye.

✉ Corresponding authors:

Alexandra Zahradníková, alexandra.zahradnikova@savba.sk

Ivan Zahradník, ivan.zahradnik@savba.sk

Short title: RyR channel operation by divalent ions

Abstract

Ryanodine receptors (RyRs) serve for excitation-contraction coupling in skeletal and cardiac muscle cells in a noticeably different way, not fully understood at the molecular level. We addressed the structure of skeletal (RyR1) and cardiac (RyR2) isoforms relevant to the gating by divalent ions (M^{2+}). The bioinformatics analysis of 43 cryo-EM RyR structures ascertained the EF1 and EF2 loops as a moderate-affinity non-specific M^{2+} binding site both in RyR1 and RyR2. The EF1/EF2 loops were allosterically coupled to the S6 gate by two parallel pathways. The intra-monomeric pathway uses the U-motif, ATP binding site, S45 linker, and S6 helix, shared with the Ca^{2+}-activation pathway in both RyR isoforms. The inter-monomeric pathway, prominent in RyR1, passes through the S23* loop of the neighbor monomer (*) and *via* the U-motif* to the S6* gate either directly or through the S45* linker or the caffeine binding site (CFF*). The structural pieces of evidence for the M^{2+}-binding activation and inhibition sites and their interacting allosteric networks were implemented in the model of RyR operation based on statistical mechanics, Monod-Wyman-Changeaux theorem, and Markov processes. This model defines allosterically coupled closed, open, and inactivated RyR macrostates common for both RyR isoforms and solves the relative occupancy of macrostates in dependence on cytosolic M^{2+} concentrations. The model approximated the single-channel open probability data for RyR1 and RyR2 of several species obtained in the presence or absence of ATP and luminal calcium. The proposed platform of RyR operation interprets the structural and functional data of mammalian RyR channels on common grounds.

Keywords:

RyR channel; striated muscle; structure-function; ion-binding site; allosteric pathway; open probability; activation; inactivation.

Introduction

Ryanodine receptor (RyR) plays a central role in the calcium-dependent functions of excitable cells. RyRs reside on the membrane of the endoplasmic/sarcoplasmic reticulum (ER/SR) and upon cell excitation, they control the release of calcium ions from the ER/SR lumen to cytosol. Three RyR isoforms are expressed in mammals: RyR1 in skeletal muscle cells, RyR2 in cardiomyocytes, neurons, and endocrine cells, and RyR3 in many tissues at lower levels (Meissner, 2017). Although RyR isoforms differ substantially in their sequence, function, and role in different tissue types, they show almost identical molecular architecture (Wagenknecht and Samso, 2002). All three RyR isoforms form a homo-tetrameric transmembrane channel, which harbors multiple regulatory sites, mostly at their cytosolic side (Meissner, 2017). It is important to note that, with a few exceptions, the regulatory binding sites reside on the monomer, so there are 4 equivalent binding sites of each type per RyR tetramer. Consequently, individuals heterozygous for a congenital mutation in the RyR gene have an equal abundance of mutated and wild-type monomers, which combine at random into tetramers (Zahradnik et al., 2005; Wilson et al., 2021).

Specific ligand-binding sites have been found for natural activators Ca^{2+}, ATP, and xanthines (des Georges et al., 2016; Chi et al., 2019; Melville et al., 2022a; Miotto et al., 2022); for regulatory molecules like calstabins and calmodulin (des Georges et al., 2016; Gong et al., 2019; Woll et al., 2021), the diamide insecticide chlorantraniliprole (Ma et al., 2020); and for emerging clinically important stabilizers like Rycals (Melville et al., 2022a; Miotto et al., 2022). RyR activators ryanodine and imperacalcin have binding sites inside the conduction pathway common to the whole RyR tetramer (des Georges et al., 2016; Haji-Ghassemi et al., 2023). Many other regulatory sites need to be revealed for regulators such as dantrolene, junctin, triadin, luminal Ca^{2+}, calsequestrin, etc. The modulation of RyR activity by phosphorylation, oxidation, nitrosylation, etc., is of importance but only the effects of PKA phosphorylation on RyR2 structure have been studied up to date (Miotto et al., 2022).

The molecular architecture as well as the localization of mutations that compromise RyR function is very similar among isoforms. Most known mutations cause muscle conditions that may have fatal consequences in the case of cardiac muscle (Robinson et al., 2006; Sleiman et al., 2021). Over two hundred mutations that cause dysregulation of calcium release are localized mainly in four specific regions of the RyR monomer (Ikemoto and Yamamoto, 2000; Robinson et al., 2006; George et al., 2007; Iyer et al., 2023). These mutations are typically characterized by the increased sensitivity of calcium release to cytosolic and/or luminal calcium, by the decreased sensitivity to inactivation by high cytosolic concentrations of magnesium or calcium, or by increased basal RyR activity (Lehnart et al., 2004; Witherspoon and Meilleur, 2016; Guo et al., 2020; Sleiman et al., 2021; Wilson et al., 2021).

The complex structure of RyR tetramer may adopt a large number of configurations (des Georges et al., 2016; Dashti et al., 2020). In RyR1, four discrete structural states were discerned under different cytosolic conditions - closed (C), primed (P), open (O), and inactivated (I) (des Georges et al., 2016; Nayak and Samso, 2022; Nayak et al., 2024). With increasing concentrations of the activators (Ca^{2+}, ATP derivatives, or xanthine derivatives), the configuration of the tetramers shifted from the closed state to the primed and open state (des Georges et al., 2016; Dashti et al., 2020). At a very high Ca^{2+} or Mg^{2+} concentration, the inactivated state was observed (Nayak and Samso, 2022; Nayak et al., 2024). Under

similar conditions, analogous C, P, and O states were observed also in RyR2 (Chi et al., 2019); unfortunately, the structure of RyR2 in the inactivated state has not been published yet.

Upon transition from the closed state to either primed, open, or inactivated states, the large cytoplasmic shell moves downward and outward (des Georges et al., 2016; Steele and Samso, 2019; Miotto et al., 2022), a movement that transpires as a progressively more negative flexion angle (Steele and Samso, 2019), and the Central and C-terminal domains rotate against each other in each monomer (Nayak and Samso, 2022). The overall structure of the primed and inactivated states resembles more the open than the closed state but the ion conduction pore is closed (des Georges, 2016 #5; Chi, 2019 #15; Nayak, 2022 #48).

In striated muscle cells, RyR channels cluster at the discrete sites of sarcoplasmic reticulum attached to the sarcolemma in triads or dyads, where electrical excitation triggers transient calcium release by activation of RyRs. Activation mechanisms differ between skeletal and cardiac muscle cells. *In situ*, RyR1 channels are open by direct coupling to the $Ca_v1.1$ channels, while RyR2 channels are activated by binding calcium ions injected through the $Ca_v1.2$ channels (Rios and Stern, 1997). In isolation, however, the RyR1 and RyR2 channels are activated by Ca^{2+} ions equally well (Chu et al., 1993). The activation calcium-binding site was structurally identified in both RyR1 and RyR2 (des Georges et al., 2016; Chi et al., 2019).

The termination of RyR activity in situ is not fully understood (Schneider and Simon, 1988; Stern, 1992; Stern et al., 1997). In skeletal muscle cells, calcium-dependent inactivation of RyR1 is generally accepted as the major termination mechanism (Schneider and Simon, 1988). In cardiac muscle cells, the termination of RyR activity is less clear since the calcium-dependent RyR2 inactivation is weaker than that of RyR1; nevertheless, divalent ions (M^{2+}) are involved in the RyR2 inactivation/inhibition as well (Gillespie and Fill, 2013; Laver et al., 2013; Niggli et al., 2013; Gillespie, 2020; Iaparov et al., 2022).

In both RyR1 and RyR2 isoforms, Mg^{2+} ions decrease the intensity of calcium release in a concentration-dependent manner. In isolated RyRs, Mg^{2+} ions lead to an increase of the EC50 and a reduction of the maximum of RyR activation by Ca^{2+} (Laver et al., 1997; Zahradnikova et al., 2003; Iaparov et al., 2022). Ca^{2+} and Mg^{2+} have a similar inhibitory potency on the open probability in both RyR1 and RyR2 (Laver et al., 1997). This indicates the presence of a non-specific divalent ion-binding site in the RyR structure. Recently, mathematical modeling of the cardiac calcium release site (Iaparov et al., 2022) confirmed that Mg^{2+} ions could at the same time act as the negative competitor at the calcium activation site and as an inhibitor at the inhibition site. Although binding of Ca^{2+} or Mg^{2+} to an inhibitory binding site has not been observed yet in RyR structures, a consensus is emerging that the EF-hand loops constitute this site (Gomez et al., 2016; Zheng and Wen, 2020; Nayak et al., 2024; Chirasani et al., 2024).

The activation of RyR by agonists was shown to be accompanied by a conformational change around the Ca^{2+} binding site that leads to a decrease in the free energy of the open state and to a concomitant increase of the Ca^{2+} binding affinity of the activation site. As a result, the occurrence probability of a RyR state/conformation shifts from the closed toward the open (Dashti et al., 2020). It should be pointed out that the activation mechanism of both RyR1 and RyR2 by calcium is fundamentally identical regarding the Ca^{2+} dependence of their open probability (Chu et al., 1993). The amino acid identity and 3D

116 configuration of binding sites for Ca^{2+}, ATP, and caffeine/xanthine are equivalent in both RyR isoforms
117 (des Georges et al., 2016; Chi et al., 2019).

118 Though RyRs have similar activation mechanisms, they have different inactivation mechanisms. The
119 single-channel activity of RyR1 was inhibited by Ca^{2+} at a much lower concentration than that of RyR2
120 (Chu et al., 1993; Laver et al., 1995; Gyorke and Gyorke, 1998). Single-channel experiments provided the
121 same concentration dependence of the RyR inhibition for both Mg^{2+} and Ca^{2+} ions (M^{2+}), but a
122 substantially lower degree of inhibition in RyR2 than in RyR1 channels (Laver et al., 1997)). These
123 characteristics are opposite to the corresponding characteristics of RyR activation. Consequently, the
124 underlying structures and mechanisms are expected to be principally different, which is puzzling since
125 the equivalent components of RyR isoforms are similar. Moreover, the pore of the RyR tetramer is lined,
126 limited, and gated by the quadruplet of S6 segments; thus, one gating site executes both the activation
127 and the inactivation. Obviously, there is a paradox in RyR channels that equivalent structures execute
128 the activation similarly but the inactivation differently in RyR1 and RyR2.

129 The regulatory domains involved in both, the activation and inactivation of RyRs (Figure 1) are located in
130 the C-terminal quarter of the RyR. The Central domain participates in the Ca^{2+} binding activation site; the
131 C-terminal domain bears several residues of Ca-, ATP- and caffeine-binding activation sites; the U-motif
132 participates at the ATP- and caffeine-binding sites; the EF-hand region contains the putative Ca-binding
133 pair EF1 and EF2; and the S23 loop bears one residue of the caffeine-binding site and two residues
134 interacting with the EF-hand region of a neighboring monomer (Samso, 2017; Hadiatullah et al., 2022).

135 Recent studies reporting RyR structure at a high divalent ion concentration provide only indirect support
136 for the molecular mechanism of Ca^{2+}/Mg^{2+}-dependent inactivation. Wei et al. (2016) and Nayak et al.
137 (2004) observed a change in the conformation of the RyR1 EF-hands in the presence of 100 µM Ca^{2+} and
138 10 mM Mg^{2+}, respectively, compared to low-calcium or low-magnesium conditions. The RyR1 structures
139 7tdg, 7tdi, 7tdj, and 7tdk determined at 3.7 mM Ca^{2+} were proposed to represent the inactivated state
140 since they showed the conduction pore closed (diameter of ≈11 Å at Cα atoms of I4937) (Nayak and
141 Samso, 2022). Importantly, the 7tdh structure obtained in parallel under the same conditions showed
142 the pore open (diameter of 14.3 Å) (Nayak and Samso, 2022) indicating that RyR may attain two
143 different states under the same conditions. This could explain in part why the RyR2 structure 6jiy
144 obtained at 5 mM Ca^{2+} had the pore open (diameter of 17 Å) (Gong et al., 2019), at odds with the
145 expectation to find the channel in the inactivated state with a closed pore at so high Ca^{2+} concentration.
146 Confoundingly, even at 3.7 mM Ca^{2+} or 5-10 mM Mg^{2+} concentrations in the reconstitution media the Ca
147 or Mg atoms were observed only at the Ca-activation site, near the bound ATP molecule, or in the ion
148 flux pathway of RyR1 but not elsewhere (Nayak and Samso, 2022; Nayak et al., 2024). This indicates that
149 the potential inhibition site has an affinity for divalent ions smaller than ATP (K_d ≈200 µM, (Bers et al.,
150 1994)).

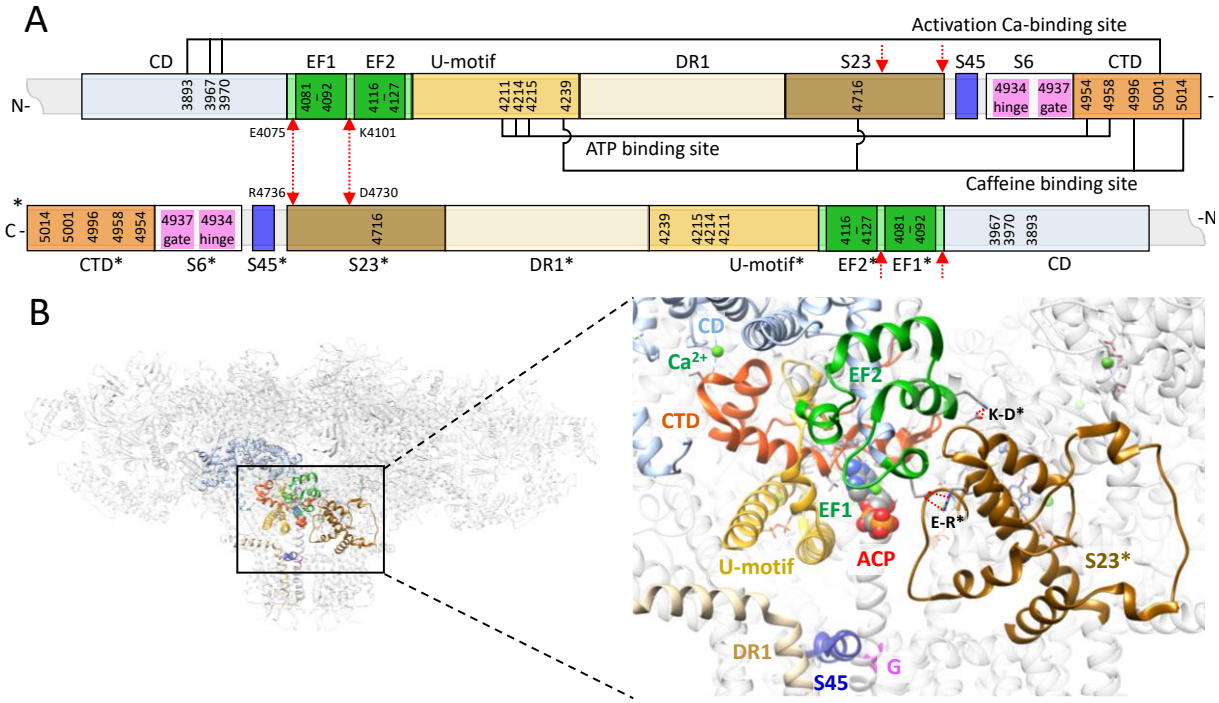

Figure 1. The sequences and the molecular structures related to the RyR channel operation.
A: The block scheme of the rRyR1 C-terminal quarter (3667-5037) for two neighbor monomers. Light blue - the Central domain (CD); light green - the EF-hand region; dark green - EF1 and EF2 motifs; tan – the Divergent region 1 (DR1); yellow - U-motif; light brown - S23 loop; blue – S45 linker (S45); white - the S6 segment with the hinge and gate residues in magenta; orange - the C-terminal domain (CTD). Red arrows – salt bridges between interacting residues of the EF-hand region and the S23* loop. The asterisks indicate a reference to the neighbor RyR monomer located counterclockwise in the top view of the channel. The connectors connect the canonical amino acid residues of the indicated binding sites. **B: Left** – the see-through side view of a RyR1 tetramer (Ca-inactivated state, rabbit 7tdg (Nayak and Samso, 2022)); top – the cytoplasmic side, bottom – the SR luminal side. **Right** - the detail of regions involved in the RyR operation. Colors correspond to A. Green spheres - Ca atoms at the activation binding sites, and at the ACP (adenosine 5'-[β,γ-methylene]triphosphate) molecule bound at the ATP site (center). The brown color indicates the S23* loop of the neighbor monomer. The short red dotted lines correspond to the salt bridges between residues K4101-D4730* and E4075-R4736* (red arrows in A). G - the hinge and gate residues D4934 and I4937 of the S6 segment.

Another region that seems to play a role in divalent-ion-dependent inactivation is the S23 loop. Three amino acids (R4736, Y4733, G4732) of the S23 loop were proposed as important components of Ca^{2+}-dependent inhibition in rabbit RyR1 (Gomez et al., 2016). Their mutation induces malignant hyperthermia (MH) and increases the IC50 for calcium-dependent inhibition. Indicatively, the S23 loop was found nearer the EF-hand region of the adjacent monomer in the RyR1 structure obtained at 10 mM Ca^{2+} than in the structure at <0.1 μM Ca^{2+} (Efremov et al., 2015) and they were connected by salt bridges in the inactivated RyR1 structure but not in the open RyR1 structure determined under the same conditions (Nayak and Samso, 2022). Taking together the findings mentioned above, it may be concluded that the EF-hand region is a serious candidate for the RyR inhibition site; however, a functional or structural explanation of the differences between the RyR1 and RyR2 inhibition was not revealed. Part of the problem is in the relatively low resolution of the EF-hand region in cryo-EM structural studies.

163 Another RyR region that was shown to participate in the regulation of RyR activity is the S45 linker
164 (amino acid residues 4820-4833 in rRyR1). Alanine substitution of residues T4825 or S4829 in RyR1
165 decreased its sensitivity to caffeine, the maximum of the open probability, and the maximum of
166 ryanodine binding, while the mutation L4827A and the MH-linked mutation T4825I increased both
167 maxima (Murayama et al., 2011). Moreover, the MH mutations T4825I and H4832Y were reported to
168 increase the IC50 of RyR1 to inactivation by Ca^{2+} (Gomez et al., 2016). Thus, this segment plays a role in
169 both the activation and the inactivation of the ryanodine receptor.

170 Most of the published RyR structures were collected under experimental conditions that vary between
171 laboratories. As a result, the electron density maps vary and deductions inferred from individual maps
172 and structural models may not be equally valid for particular aspects. Similar problems occurred with
173 recordings and interpretation of functional experiments. The question arises as to whether these are
174 even compatible. If yes, it should be possible to construct a functional model from structural data that
175 would explain functional data. To this aim, we selected a large set of published RyR1 and RyR2
176 structures determined under conditions comparable with relevant single-channel experiments and
177 estimated relationships between divalent ion binding and signaling pathways. We focused on the
178 allosteric mechanism of RyR control by divalent ions, with the use of bioinformatic and structural
179 analysis methods. We compare RyR1 and RyR2 structures and construct a fundamental allosteric
180 mechanism common for both RyR isoforms. The proposed mechanism is verified by an operational
181 model of the RyR channel open probability based on the MWC theory (Monod et al., 1965) and
182 statistical mechanics (Marzen et al., 2013).

183 # Results

184 To correlate the structure of RyR with its function we took advantage of published RyR structures and
185 RyR open probabilities obtained under similar conditions. RyR structures selected for analysis were
186 obtained under conditions stabilizing the closed, primed, open, or inactivated structural states. RyR2
187 structures of the inactivated state have not been published yet. Open probabilities of both RyR1 and
188 RyR2 selected for analysis were determined at Ca^{2+} and Mg^{2+} concentrations causing activation and
189 inhibition of RyRs. All structures and open probabilities analyzed here are listed in Extended View Table
190 S1.

191 Below we first examine the molecular structure of the EF-hand pair EF1/EF2, the candidate inhibition
192 site, for its propensity to bind divalent ions. Second, we analyze the spatial interaction between the EF-
193 hand region and the S23 loop, the proposed inactivation path. Third, we evaluate the relative positions
194 of the RyR central core domains relevant to the RyR single-channel activity regulation, in all examined
195 RyR states and isoforms. Fourth, we identify the allosteric network in both RyR isoforms from the
196 regulatory allosteric sites to the channel gate for the representative RyR states. Fifth, we construct a
197 comprehensive model of RyR operation and use it to calculate the dependences of RyR1 and RyR2 open
198 probabilities on the divalent ion concentration. Finally, we compare the model predictions with the
199 relevant single-channel open probability data.

200 ## 1 The propensity of EF1 and EF2 loops to bind divalent ions

201 In all RyR structures, EF1 and EF2 have a form of a typical EF-hand pair, similar to Ca-binding sites of
202 specialized Ca-binding proteins. To evaluate and compare their ability to bind divalent ions we used the
203 identity score (IS) of EF-hand loops (see Methods), which has a maximum value of 12/6/3 (21) for
204 calmodulin. The sequence of the EF1 loop in RyR1, VTDPRGLISKKD, the same in all examined mammals
205 (rabbit, rat, mouse, human, dog, and pig), has IS of 10/4/2 (16). The corresponding EF1 loop sequence
206 for RyR2 is DPDGKGIISKRD for the rabbit and DPDGKGVISKRD for the other examined mammals, both
207 having IS of 11/5/3 (18), by 2 points higher than for the EF1 of RyR1. The sequence of the EF2 loop is
208 EADENEMINCEE in human, mouse, and rat RyR1; EADENEMINFEE in rabbit RyR1, and EADENEMIDCEE in
209 pig RyR1, while in RyR2 it is ETDENETLDYEE in all examined species. All EF2 sequences have an IS of
210 10/5/2 (17). The identity score of the scrambled RyR1 EF1 sequence YDGDKPSKLDIT (Fessenden et al.,
211 2004) is 9/4/2 (15), that is, by 1 point lower than that of EF1 in WT RyR1. The scores of EF1 and EF2 are
212 comparable with the calmodulin EF-hand sequence score of 12/6/3 (21) suggesting that both the EF1
213 and EF2 loops and even the scrambled EF1 loop can bind divalent ions but probably with a reduced
214 affinity and selectivity.

215 We examined the theoretical ion binding ability of EF1 and EF2 hands in the region corresponding to
216 rRyR1 residues 4063-4196, which starts ahead of the EF-hand region and ends behind the U-motif onset,
217 to keep the secondary structure intact. This region was extracted from 10 recent RyR1 and RyR2
218 structures specified in Expanded View Dataset EV1. The scrambled versions of EF1 were created using
219 RyR structures determined at high Ca^{2+} concentration (Nayak and Samso, 2022), in which the wild-type
220 EF1 sequence of amino acids 4079-4092 was replaced by the scrambled sequence YDGDKPSKLDITRV
221 that showed RyR2-type inactivation in experiments (Fessenden et al., 2004). Finally, all structures

222 corresponding to rRyR1 residues 4063-4196 were subjected to energy minimization and submitted to
223 the MIB2 server (Lu et al., 2022) for evaluation of the ion binding score (IBS) of individual amino acid
224 residues and the number of ion binding poses (NIBP) for Ca and Mg ions. IBS values of individual
225 residues are determined using sequence and structure conservation comparison with 409 and 209
226 respective templates from the PDB database for Ca^{2+} and Mg^{2+} (Lin et al., 2016) and assessing the
227 similarity of the configuration of the residue to its configurations in known structures of its complexes
228 with the given metal (Lu et al., 2012). Ion binding sites are determined by locally aligning the query
229 protein with the metal ion-binding templates and calculating its score as the RMSD-weighted scoring
230 function Z. The site is accepted if it has a scoring function Z>1, and based on the local 3D structure
231 alignment between the query protein and the metal ion-binding template, the metal ion in the template
232 is transformed into the query protein structure (Lin et al., 2016). The larger the IBS value, the higher the
233 tendency of the residue to bind the ion. The larger the NIBP value, the larger the number of such
234 complexes with an acceptable structure. The IBSs were estimated for amino acid residues 1, 3, 5, 7, 9,
235 and 12 of the EF1 and EF2 loops involved in ion binding. As a comparison baseline, we used the residues
236 of 4063-4196 without the 12 metal-binding residues. The number of IBPs was determined as the
237 number of all poses that involved at least 2 residues of the ion binding loops. Table 1 presents statistics
238 on IBS and NIBP data.

239 The IBS values of the ion-binding residues of both EF1 and EF2 were significantly larger than the IBS
240 values of the remaining residues (KWANOVA, $p < 0.001$). ANOVA analysis indicated that IBS of EF1 for
241 Ca^{2+} ions was significantly higher in RyR1 and RyR2 than in the RyR1scr structures ($p = 0.0128$ and
242 $p < 0.001$) but for Mg^{2+} ions only the difference between RyR2 and RyRscr was significant ($p < 0.001$). EF1
243 and EF2 bind Ca^{2+} equally in both isoforms. In RyR2, EF2 binds Mg^{2+} more strongly than EF1 ($p = 0.0028$)
244 while in RyR1 both EF hands bind Mg^{2+} equally. Importantly, however, the EF1 had an IBS for Ca^{2+} and
245 Mg^{2+} significantly larger in RyR2 than in RyR1 ($p = 0.0011$ and 0.0014, respectively). The extent of these
246 differences can be assessed by comparison with calmodulin (Table 1), which also possesses two pairs of
247 EF-hands that bind M^{2+}, albeit with micromolar affinity. The lower IBS values of EF-hands in RyRs are
248 consistent with the observed sub-millimolar concentration range of inhibitory potency of Ca^{2+} and Mg^{2+}
249 in RyR isoforms.

Table 1. The ion-binding ability of EF1 and EF2 in RyR isoforms.

Structure	N	IBS (mean ± SEM)						NIBP (mean ± SEM)			
		EF1		EF2		Baseline		EF1		EF2	
		Ca	Mg	Ca	Mg	Ca	Mg	Ca	Mg	Ca	Mg
RyR1	10	0.7±0.1	0.4±0.1	0.8±0.2	0.8±0.1	-0.07±0.03	-0.06±0.03	1.9±0.4	0.7±0.3	4.3±1.4	2.4±0.8
RyR2	10	1.2±0.1	1.1±0.1	1.5±0.2	1.7±0.1	-0.14±0.03	-0.13±0.03	6.6±1.8	2.1±0.4	9.3±2.3	5.1±1.4
RyR1scr	7	0.2±0.1	0.2±0.1	0.7±0.1	0.7±0.1	-0.04±0.03	-0.04±0.03	0.7±0.4	0.9±0.3	2.1±0.7	1.7±0.6
CaM-N	1	2.3	2.2	2.3	2.2	-0.42	-0.41	56	8	42	5
CaM-C	1	1.6	2.0	1.8	1.8	-0.37	-0.39	8	4	37	7

IBS - ion binding score. NIBP - ion binding poses. N – the number of evaluated RyR structures. RyR1scr stays for the RyR1 with scrambled EF1-hand sequence. CaM-N and CaM-C stay for the N-terminal and C-terminal EF-hand pairs of calmodulin, respectively. The values for calmodulin were estimated using the structure 1exr (Wilson and Brunger, 2000).

250 The estimates of NIBPs (Table 1) emphasize findings on IBS of the RyR1 and RyR2 EF-hands, regarding
251 their sensitivity to the type of divalent ion. As demonstrated, the NIBP of CaM-N and CaM-C for Ca^{2+} is

252 markedly higher than that for Mg^{2+}, in agreement with the known selectivity of calmodulin for these
253 ions. In both EF1 and EF2 of RyRs, the difference in NIBP of Ca^{2+} and Mg^{2+} is small, indicating low
254 selectivity for divalent ions. Comparison of NIBP in RyR isoforms indicates a better binding of M^{2+} in
255 RyR2 than in RyR1. The structures with scrambled EF1 loop returned lower values of IBS and NIBP.

256 The lower IS, IBS, and NIBP values of the scrambled RyR1 structures are in agreement with the
257 decreased Ca^{2+} inhibitory potency of the scrambled EF1-hand RyR1 construct (Fessenden et al., 2004).
258 The higher IBS and NIBP for Ca^{2+} and Mg^{2+} of the EF1-hand in RyR2 than in RyR1 is at odds with the
259 weaker inhibition of ^{3}H-ryanodine binding by Ca^{2+} ions in RyR1 channels with their EF1 motif exchanged
260 for the RyR2 counterpart (Gomez and Yamaguchi, 2014), suggesting that the effect of this exchange
261 cannot be caused by the higher Ca^{2+} affinity of the EF1 loop in RyR1 than in RyR2.

262 The EF2 of RyR2 has the same IS but somewhat higher IBS and NIBP values than the EF2 of RyR1. This
263 theoretical result is in line with the lack of the effect of the exchange of the RyR1 region around the EF2
264 for the corresponding RyR2 region on the Ca^{2+}-dependent inhibition of ryanodine binding (Gomez and
265 Yamaguchi, 2014), meaning that the difference between Ca-dependent inactivation of RyR1 and RyR2 is
266 not caused by the properties of the EF2 hand.

267 To summarize, the theoretical ion binding results provided no support for the hypothesis that the
268 difference between RyR isoforms comes from the different affinity of their putative inhibitory sites to
269 divalent ions. On the contrary, they indicate a substantial ability of EF1 and EF2 to bind divalent ions, a
270 prerequisite to constitute the inhibitory Ca-binding site.

271 2 Spatial interactions between the EF-hand and S23* regions

272 As we reasoned above, the difference in the propensity of the EF-hand region to bind divalent ions
273 cannot explain the difference in the Ca-dependent inactivation between RyR isoforms. The question is
274 then whether the difference can reside in the transmission of the ion-binding signal from the EF-hands
275 to the channel gates. A clue was provided by Gomez et al. (2016) who found that malignant
276 hyperthermia mutations of three amino acids of the S23 loop shifted the inhibition of ryanodine binding
277 in RyR1 to a higher Ca^{2+} concentration, close to that of the RyR2, and proposed that these three amino
278 acids are involved in the inter-monomeric interaction of the S23* loop with the EF-hand region (Gomez
279 et al., 2016). Nayak and Samsó (Nayak and Samso, 2022) measured the distance between the EF-hand
280 region and the S23* loop as the distance between pairs of residues allowing direct interaction at
281 sufficient proximity. These included glutamate E4075 to arginine R4736* (distance D1) and lysine K4101
282 to aspartate D4730* (distance D2) in rabbit RyR1 structures. Both distances showed a tendency to
283 decrease among RyR1 structures in the order closed (7k0t) > open (7tdh) > primed (5taq) ≈ Ca-
284 inactivated (7tdg), indicating that these two pairs of residues may play a role in RyR1 inhibition (Nayak
285 and Samso, 2022). We measured both distances in the whole set of RyR structures to examine the
286 difference between the RyR isoforms.

287 The D1 distances measured between Cα atoms of the E4075-R4736* pair are summarized in Figure 2,
288 and compared with the theoretical estimate of the maximal distance allowing their interaction. The
289 median of D1 values measured in the RyR1-C structures is too large for the residues to interact, while

290 those of the open, primed, or inactivated RyR1 structures are in the range allowing for proper
291 interaction between residues in a suitable rotamer configuration. Of interest is the RyR1-Mg structure
292 7umz, defined as "ACP/10mM free Mg^{2+}-closed state" (Nayak et al., 2024), obtained at a very high
293 concentration of Mg^{2+} ions that are supposed to stabilize the inactivated state (Laver et al., 1997). This
294 structure provided D1 similar to those found in primed, open, and inactivated states. The D1
295 measurements in RyR2 structures provided completely different results. In all RyR2 states the median
296 D1 is substantially larger than that in RyR1 and, importantly, also larger than the maximum interaction
297 distance estimated for hRyR2 D4030-R4665* (the equivalent of rRyR1 E4075-R4736*).

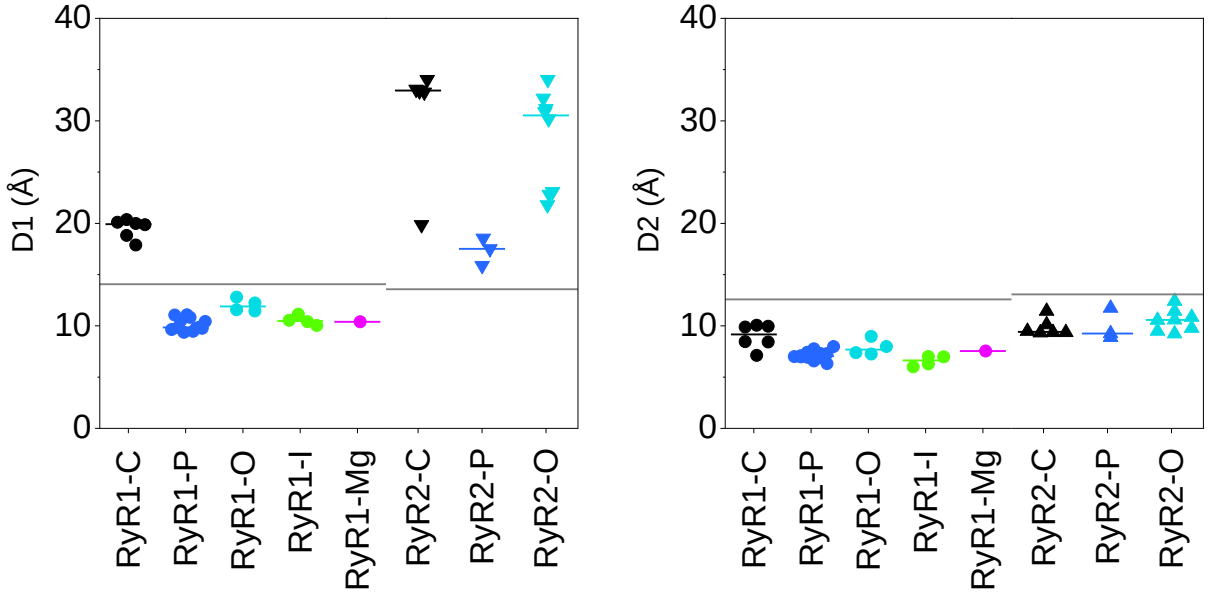

Figure 2. **Distances between key amino acid pairs of the EF-hand and S23* in RyR structures. Left** – Distances D1 between the Cα atoms of E4075 and R4736* or equivalent. **Right** - Distances D2 between the Cα atoms of K4101 and D4730* or equivalent. Circles - RyR1 states. Triangles - RyR2 states. C – closed state, black symbols. P – primed state, blue symbols. O – open state, cyan symbols. I – inactivated state, green symbols. Mg – high-magnesium state, magenta symbols. Short lines - the median values of groups. Long lines – the theoretical maximum distances allowing H-bond formation.

298 Measurements of D2 distances yielded only subtle distinctions between RyR structures (Figure 2, right).
299 In all RyR1 structures, the median D2 values were neither substantially nor statistically different. In all
300 RyR1 states, the K4101-D4730* separation allowed for proper residue interaction by H-bonds. In RyR2
301 structures, the D2 medians of individual states were only slightly larger than those in the respective
302 RyR1 structures, much less so than in the case of D1 distances. The D2 medians of closed, open, and
303 primed RyR2 states were similar and in the theoretical H-bond interaction range.

304 These results indicate that the glutamate-arginine* (E4075 and R4736*) distance D1 between the EF-
305 hand and S23* regions is too large in all RyR2 structures, in contrast to the RyR1 non-closed states
306 including the inactivated state, in which the residues may potentially interact and transmit the binding
307 signal. On the other hand, the D2 distances in all RyR1 and RyR2 structures assume values that may
308 allow interaction of the lysine with the aspartate* (K4101-D4730*) in RyR1 or with the glutamate* in
309 RyR2, and thus potentially participate in signal transmission.

The resolution of published cryo-EM RyR structures is typically about 3-4 Å, which limits conclusions based only on estimates of specific interaction distances. Moreover, we cannot exclude the presence of interactions among other residues. A more robust measure of domain interactions could be the contact area between the juxtaposed surfaces of the EF-hand region and the S23* loop, and the number of possible electrostatic interactions (H-bonds and salt bridges) between their residues on the same set of RyR1 and RyR2 structures. For this purpose, the motifs corresponding to rabbit RyR1 residues E4032 – E4182 of one monomer, and to rabbit RyR1 residues D4695 - L4745 of the neighboring counterclockwise monomer were cut out from the corresponding RyR structures, optimized, and submitted to the PDBePISA server (see Methods for details). The results, summarized for all analyzed structures in Figure 3, point to a substantially larger contact area and number of interactions in primed, open, and inactivated RyR1 structures than in closed RyR1 and closed, primed, and open RyR2 structures, in line with the distance measurements presented above. The RyR1-Mg structure 7umz (Nayak et al., 2024), provided both values similar to those found in primed, open, and inactivated states. The contact area and the number of electrostatic interactions correlate more steeply in RyR1 than in RyR2 structures. This indicates that the spatial arrangement of the two domains in RyR2 structures does not support the formation of electrostatic interactions as efficiently as in RyR1 structures, even if the two domains are near each other.

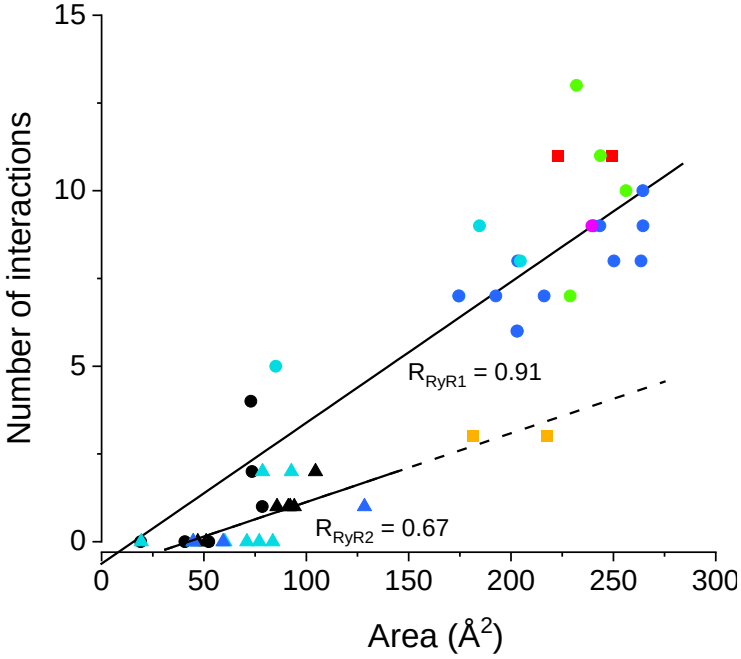

Figure 3. Number of interactions and area between the EF-hand region and S23* loop in RyR structures. Circles - RyR1 structures; Triangles - RyR2 structures; Black - closed state; Blue – primed state; Cyan – open state; Green - inactivated state; Magenta – high-Mg state. Orange squares - inactivated RyR1 with MH mutations R4736W, R4736Q; Red squares - inactivated RyR1 with MH mutations G4733E, F4732D. R_{RyR1}, R_{RyR2} - Pearson's correlation coefficients for RyR1 and RyR2 data groups (solid lines); n_{RyR1} = 27; n_{RyR2} = 17; $p < 0.005$ in both cases). Note: the correlations were calculated without the data for mutated structures (squares). The dashed line extrapolates the correlation line.

After optimization, 24 out of 27 RyR1 structures formed H-bonds and/or salt bridges between at least one of the residue pairs Q4100-I4731*, (E4075/D4079)-R4736*, (Q4100/K4101)-D4730* in all RyR1 states. The maximum number of simultaneous hydrogen bonds detected by the PDBePISA server was 6. On the other hand, in the corresponding RyR2 structures only 8 out of the 17 analyzed structures formed interactions between EF-hand - S23* residue pairs, with a maximum of two hydrogen bonds in a single structure. Moreover, the EF-hand aspartate and glutamate (corresponding to E4075 and D4079 in RyR1) could not form contact with the arginine corresponding to rRyR1 R4736*, the key S23* residue, in any RyR2 structure. These data suggest that interactions between the basic arginine residue R4736* and

335 the acidic residues E4075 and D4079 are specific for Ca^{2+}-dependent inactivation in RyR1, whereas the
336 interactions between the lysine K4101 and the residues D4730* and I4731* (rRyR1 notation) may play a
337 part in the inactivation of both RyR1 and RyR2 isoforms.

338 Interestingly, the replacement of arginine R4736* for tryptophan or glutamine in RyR1 that alleviates
339 RyR1 inhibition by Ca^{2+} (Gomez et al., 2016) provided a reduced number of interactions per interaction
340 area (Figure 3, orange squares), similar to that predicted for RyR2 type interaction. However,
341 replacements of glycine G4733* for glutamate and phenylalanine F4732* for aspartate, also known to
342 alleviate RyR1 inhibition by Ca^{2+} (Gomez et al., 2016) did not affect the number of interactions (Figure 3,
343 red squares). This means that the electron donor residue arginine R4736* is probably important for the
344 transmission of the divalent ion binding signal from the EF-hands to the S23* loop in RyR1. On the other
345 hand, the mutations G4733E and F4732D, both introducing a negative charge on S23, may act by
346 neutralizing the positive charge of R4736 thus making the transmission less effective without changing
347 the number of possible interactions.

348 3 Relative positions of the RyR core domains

349 The above distance analyses suggested clearly that the relative positions of the EF-hand and S23* loop
350 are state- and isoform-specific, and thus may affect the propensity of RyR1 and RyR2 for M^{2+}-dependent
351 inactivation. Additional contributions to the inactivation could arise from other domains involved in the
352 signal transmission that may assume different relative positions and shapes in specific RyR states and
353 isoforms. Previous RMSD (root mean square displacement) analysis of the backbone Cα atoms revealed
354 that the position of the C-terminal domain relative to the Central domain was shifted in primed and
355 open RyR1/RyR2 structures from the position in closed structures (Miotto et al., 2022; Nayak and
356 Samso, 2022). An even higher degree of the C-terminal domain shift was present in the inactivated RyR1
357 structure 7tdg (Nayak and Samso, 2022).

358 We inspected differences in conformational states of core domains located along the C-terminal quarter
359 of the RyR monomer by means of the RMSD analysis using the same set of RyR structures as analyzed
360 above. To begin with, the analyzed RyR structure and the reference RyR structure were aligned by their
361 Central domains, selected as the aligning reference for sufficient size and well-defined state-
362 independent structure. The distances between the corresponding Cα atoms of domains of interest in the
363 tested and the reference structures were then used to calculate their $RMSD_{100}$ values. The graphs of
364 Figure 4 compare $RMSD_{100}$ estimated relative to the closed RyR1 structure 7k0t (horizontal axis) and the
365 inactivated RyR1 structure 7tdg (vertical axis). The S45 linker, known to participate in RyR gating, could
366 not be analyzed in this way since its length of 13 residues is insufficient for correct $RMSD_{100}$
367 determination (Carugo and Pongor, 2001). The $RMSD_{100}$ of domains in the same state and isoform were
368 nearly always spread within a circle with a radius of 1 Å for all RyR structures. Thus, we considered the
369 structure of a RyR region to differ between channel states if their mean $RMSD_{100}$ values differed by more
370 than 2 Å (Carugo and Pongor, 2001).

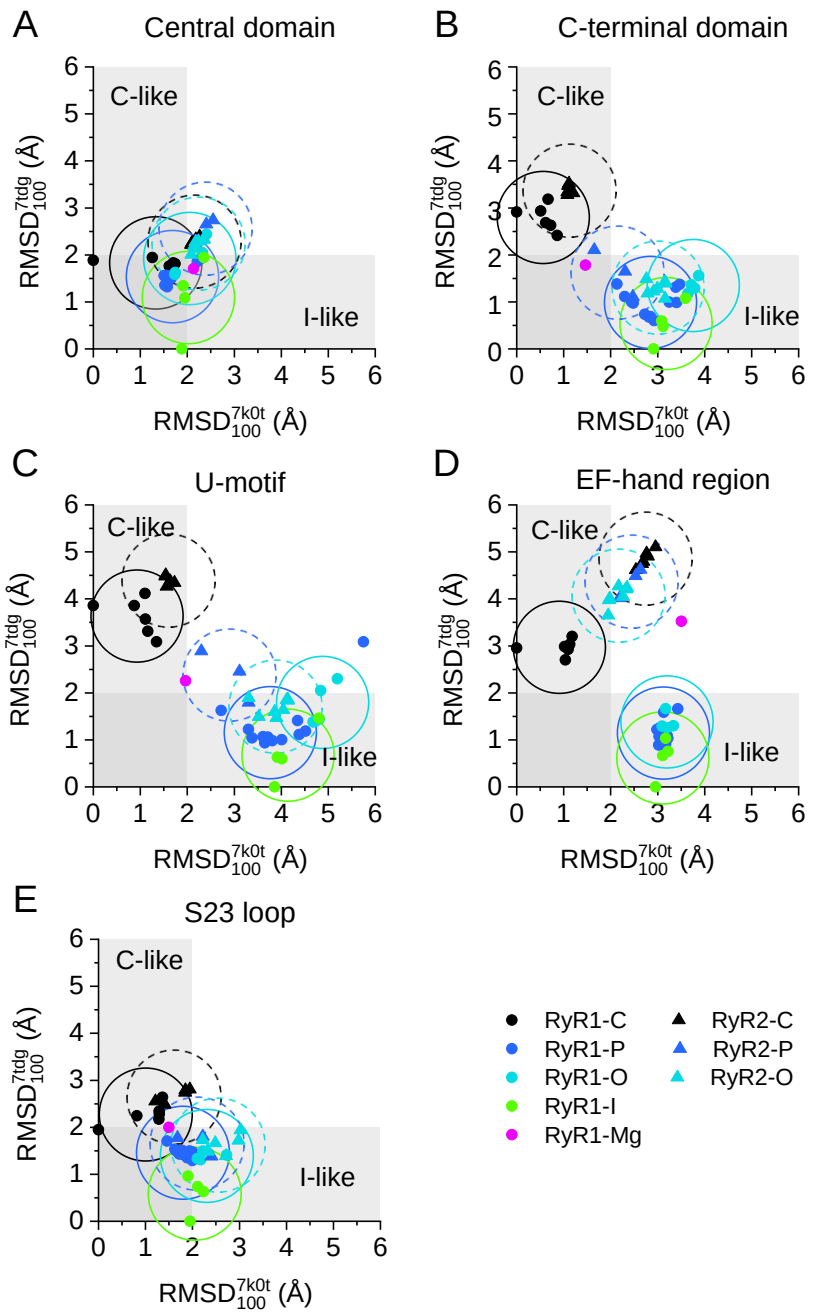

Figure 4. The RMSD analysis of RyR structures. Horizontal axis - $RMSD_{100}$ of the RyR structures relative to the closed RyR1 structure 7k0t. Vertical axis - $RMSD_{100}$ of the RyR structures relative to the inactivated RyR1 structure 7tdg. The circles of 1 Å radius are centered on the mean RMSDs of the corresponding group of RyR isoforms and states and appraise the significance of differences between groups (when the corresponding circles do not intersect the difference is significant). The solid circle data points and the solid circle lines indicate RyR1 data; The solid triangle data points and the dashed circle lines indicate RyR2 data. Colors indicate RyR states (see inset). C-like and I-like grey bands indicate the similarity of $RMSD_{100}$ values to either the closed or inactivated reference states.

Comparison of domain positions in RyR1 and RyR2 structures

The $RMSD_{100}$ values of the Central domain in all RyR structures were similar and independent of the RyR state or isoform (Figure 4 A), as required for the self-aligned reference domain.

The C-terminal domain and U-motif (Figure 4 B and C) of all RyR1-C and RyR2-C structures (black symbols) showed similar $RMSD_{100}$ values close to those of the reference closed structure (7k0t). The RyR1-I structure 7umz, obtained in the presence of high Mg^{2+} concentration, showed $RMSD_{100}$ values halfway between those of closed and inactivated RyR1 structures.

378 In almost all other RyR1 and RyR2 structures, RMSDs of these domains were similar and close to that of
379 the reference inactivated structure (7tdg). This confirms the displacement of the CTD and U-motif
380 relative to the Central domain in primed, open, and inactivated RyR1 structures, observed previously by
381 Nayak and Samso (Nayak and Samso, 2022) for the open 7tdh, primed 7tdj, and inactivated 5taq RyR1
382 structures. Moreover, it reveals qualitatively and quantitatively similar rearrangements from the closed
383 to the primed or open states in both the RyR1 and RyR2 isoforms, indicating their similar responsiveness
384 to the activation and inactivation conditions in both RyR isoforms.

385 The EF-hand domains of RyR1 and RyR2 structures displayed markedly dissimilar RMSDs. In RyR1, the
386 open, primed, and inactivated structures (colored circles) were notably different from the closed but
387 very close to the inactivated reference (RyR1) structure. The structure 7umz, obtained at a high Mg^{2+}
388 concentration, showed $RMSD_{100}$ values significantly different from both the closed and inactivated
389 reference RyR1 structures. In RyR2, the EF-hand region of all structures (triangles) also displayed notably
390 different $RMSD_{100}$ values relative to either of the reference (RyR1) structures (Figure 4 D). These data
391 reinforce the evidence of the structural differences between the EF-hands of RyR1 and RyR2 isoforms
392 indicated by the distance analysis above.

393 The RMSD values of the S23 loop in all RyR structures were low, almost the same, and similar to those of
394 both the closed and inactivated reference structures. This points to the very high structural stability of
395 the S23 loop within the RyR monomer relative to the Central domain.

396 ## Comparison of domain positions in different RyR states

397 In all domains except the EF-hand, the RMSDs of the closed RyR1 and RyR2 structures were very similar
398 irrespective of the isoform. The RMSDs of the primed, open, and inactivated RyR1 structures and the
399 open and primed RyR2 structures were also very similar but markedly different from those of the closed
400 RyR1 and RyR2 structures. However, while there is a pronounced difference between the mean $RMSD_{100}$
401 of the EF-hand in closed RyR1 structures on the one hand and the open, primed, and inactivated RyR1
402 structures, the differences between the closed, open, and primed RyR2 structures are not significant.
403 This pronounced distinction in the EF-hand position between RyR1 and RyR2 indicates that the
404 inactivation signal in RyR2 may have a lower chance of passing to the neighbor monomer. These findings
405 also indicate that in RyR1 channels, the structural prerequisites for the inactivation signaling are present
406 also in primed and open channels and that the binding of divalent ions to the inhibition site at the EF-
407 hand region may constitute the inactivation signal.

408 Whereas the relative positions of all five examined domains were similar in the primed, open, and
409 inactivated states (Figure 4), these states differed by their flexion angle (see Methods). Despite the large
410 dispersion, the medians of flexion angles showed a tendency to decrease in both RyR1 or RyR2
411 structures in the order: closed state ≥ primed state ≥ high Mg^{2+} state ≥ open state ≥ inactivated state, in
412 RyR1; closed state ≥ primed state ≥ open state, in RyR2 (see Expanded View Dataset EV1 for details).

Interaction of EF-hand region with S23 loop.

To better understand the above-disclosed difference in the displacement of the EF-hand region and S23 loop between RyR1 and RyR2 structures (Figure 4 D and E), we aligned the RyR1-O and RyR2-O model structures on their more static S23* loop (Figure 5). We compared here only the open states, since according to the distance analysis (Figure 2) the distances in the closed states are too large, the inactivated RyR2 structure is not available, and the distances D1 and D2 are similar in RyR1-O and RyR1-I. A close look at the structure of the EF-hand region (Figure 5 A) reveals substantially different conformations of the two isoforms in the segment starting just before EF1 and ending just after EF2 (residues 4052-4140 in rRyR1). In RyR2, both EF1 and EF2 are diverted downward relative to their counterparts in RyR1. As a consequence, the D4030 of RyR2 (the equivalent of E4075 in RyR1) withdraws from its interaction with S23* (Figure 5 B, C). This confirms the results of the distance analysis, namely that RyR1 structures can make hydrogen bonds between E4075 and R4736* and between K4101 and D4730*, while the corresponding RyR2 structures can make a hydrogen bond only between K4056 and E4659* but not between D4030 and R4665* (hRyR2 numbering). The difference stems most probably from the low sequence identity (52%) for the EF-hand region (rRyR1 4071-4137 and hRyR2 4026-4092). This is much less than the sequence identity of the adjacent U-motif (81%) and the Central domain (82%), at which RyR1 and RyR2 are aligned much better (Figure 5 A).

4 Allosteric pathways from the ion-binding sites to the gate.

Transmission of a signal from the regulatory site to the active site should proceed by propagation of a perturbation through a sequence of contacts between nearby residues. This principle is used in the OHM server for the detection of allosteric pathways (Wang et al., 2020). Previously, analysis of such pathways in RyR1 structures revealed how the cytosolic calcium, ATP, and caffeine activate RyR1 (Chirasani et al., 2022). Here we have used the OHM server to explore the regulatory network of both ion-dependent allosteric pathways. We will use the term “activation pathway” for the pathway commencing at the high-affinity Ca^{2+}-binding site, and “inhibition pathway” for the pathway commencing at the low-affinity, low-selectivity M^{2+}-binding site associated with the inhibition site. Both will be considered in the model of RyR operation. The term “residue importance” defines the extent to which the given residue is involved in the propagation of a perturbation from the allosteric site to the active site, i.e., the fraction of simulated perturbations transmitted through this particular residue. The more contacts are present between two residues, the higher is the probability that a perturbation will be propagated from one to the other residue.

Since the allosteric analysis requires a complete and correct structural model, only RyR structures with the best resolution and the fewest missing residues were processed (see Methods). According to these criteria we selected five RyR1 model structures (Table 2): one closed (7k0t), one primed (7tzc), two open (7m6l and 7tdh), and one inactivated (7tdg); and four RyR2 model structures: two closed (7vmm and 7ua5) and two open (7vmp and 7ua9). The structures 7tdg and 7tdh represent two RyR1 state configurations in the same sample; similarly, the structures 7ua5 and 7ua9 represent two RyR2 state configurations in the same sample (see Expanded View Dataset EV2 for the sequences and structures of the models).

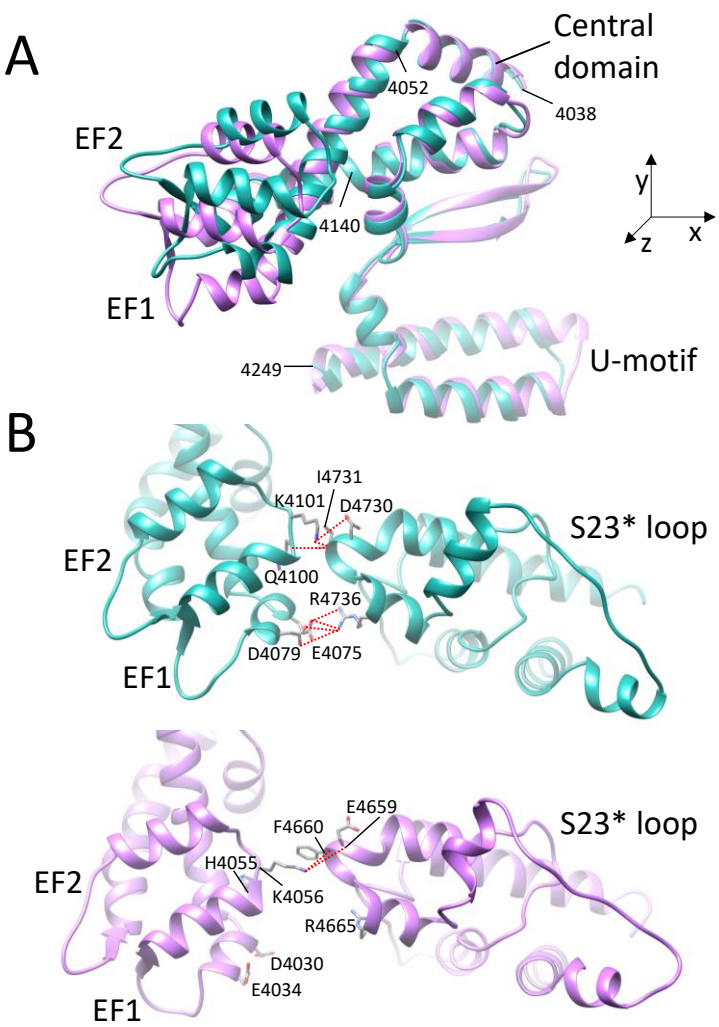

Figure 5. Structural interactions between the EF-hand and S23 in the open RyR1 and RyR2 structures. **A** – Overlay of the EF-hand region in the RyR1-O (7m6l, cyan) and RyR2-O (7ua9, magenta) structures aligned at their S23 loops (out of the image plane). Note the differences in the EF1 and EF2 positions and almost the same positions of the Central domain and U-motif segments. The RyR1 residue sequence numbers are given for orientation. **B** – Residue interactions between the EF-hand region (left) and S23* loop (right) in the RyR1-O (cyan) and RyR2-O (magenta) structures. The structures in B are rotated by 30° counterclockwise about their x, y, and z axes relative to their orientation in A. Dotted red lines -— structurally possible H-bonds between the interacting residues.

452

Table 2. **Model structures used for identifying the allosteric pathways.**

Structure	**7k0t**	**7tzc**	**7m6l**	**7tdh**	**7tdg**	**7vmm**	**7ua5**	**7vmp**	**7ua9**
Species	rabbit	rabbit	rabbit	rabbit	rabbit	mouse	human	mouse	human
RyR type	RyR1	RyR1	RyR1	RyR1	RyR1	RyR2	RyR2	RyR2	RyR2
State	closed	primed	open	open	inactivated	closed	closed	open	open
Ligands	ACP	ATP CFF Ca	ATP CFF Ca	CaACP Ca	CaACP Ca	none	ATP	 Ca	ATP XAN Ca

ACP – adenosine 5'-[β,γ-methylene]triphosphate; ATP – adenosine triphosphate; CFF – caffeine; XAN - xanthine

453 In the selected structures, we identified residues with high residue importance (RI) for both the
454 inhibition and activation network and compared them with residues important for ligand binding and
455 gating of RyR (Table 3). These residues were then identified in individual paths and the paths containing
456 identical high-RI residues were grouped. To increase the visibility of the main pathways, residues with RI
457 less than 5% of the maximum RI for the given structure were not considered. For each RyR structure,

458 this process precipitated in major pathways that shared residues of the regulatory ligand-binding sites,
459 inter-monomeric interaction sites, and the regulatory site of the S45 linker (Table 3).

Table 3. The list of important residues examined for contribution to allosteric networks.

Ligand binding sites	**Residue numbers (rabbit RyR1 numbering)** [#]
ATP binding site	**4211, 4214, 4215,** 4218, **4954, 4955**, 4957, **4958, 4959,** 4960, 4975, **4979**, 4983, **4984, 4985**
Caffeine binding site	**3753**, **4239**, 4242, 4671, **4715**, **4996**, 5011, **5014**, 5015
Interaction sites	
EF-hand region	4075, 4079, 4100, 4101
S23* loop	4730*, 4731*, 4736*
Regulatory site	
S45 linker	4821-4834

[#] Residue numbers in bold were originally defined as the ATP and CFF binding site-forming residues by (des Georges et al., 2016).
The ATP and CFF binding sites were defined as a group of residues that formed contact with a ligand in at least one of the RyR structures listed in Expanded View Dataset EV1, given that the position of a ligand in the structure is not well-defined (des Georges et al., 2016) and that not all examined model structures contained a ligand at the binding site. The interacting residues of the EF-hand– S23* regions were those identified by the PDBePISA to form a salt bridge or an H-bond between neighboring monomers in at least one RyR structure (Expanded View Dataset EV1).

460 ## The inhibition network

461 In the inhibition network analysis, we defined the ion-binding loops of the EF1 and EF2 as the allosteric
462 inhibition site (INH), and the hinge and gate of S6 and S6* as the active site (GATE). In the network
463 output list of the OHM server (see Expanded View Dataset EV2), large RI values were observed at the
464 ATP-binding residues of the U-motif and the C-terminal domain, in addition to residues next to the EF-
465 hand loops and the GATE (Figure 6). In several model structures, RIs larger than the threshold value also
466 occurred at several residues of the S45, S45*, and S23*segments.

467 Two major pathways denoted as the intra-monomeric and the inter-monomeric pathway were
468 identified in the structural models of both RyR isoforms. Both pathways displayed several branches that
469 partially fluctuated among model structures. Notably, most branches comprised residues either of the
470 ATP binding site, known to support the calcium-dependent activation (des Georges et al., 2016;
471 Chirasani et al., 2022), or of the S45 linker, known to participate in the regulation of channel gating
472 (Murayama et al., 2011; Gomez et al., 2016).

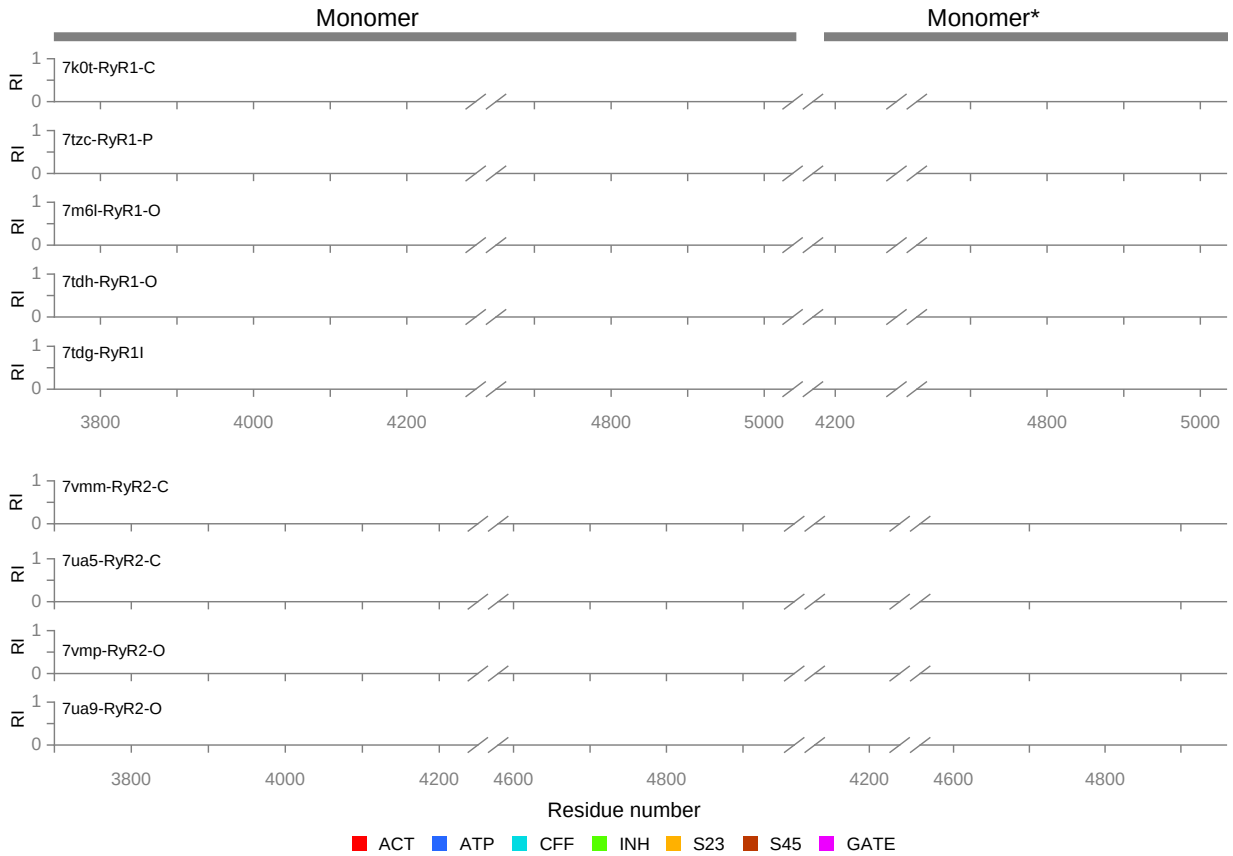

Figure 6. The residue importances in the inhibition pathways. The RIs were calculated for all detected inactivation paths and mapped on the RyR sequences. The graph displays only RI > 0.05. The color-coded marks under the sequence axis indicate the positions of important residues from Table 3 and Table 9, see the legend at the bottom, where: ACT – Ca^{2+}-binding activation site, INH – M^{2+}-binding inhibition site, ATP – ATP-binding site, CFF – caffeine/xanthine binding site, S23 – S23 loop, S45 – S45 linker, and GATE – channel gating residues.

The intra-monomeric inhibition pathway was identified in all 9 investigated model structures and represented 48 – 100 % of the first 100 inactivation paths generated by OHM for individual model structures (see Expanded View Dataset EV2). In both RyR isoforms, this pathway was formed by six major branches (I1 – I6, Table 4; Appendix Table S1) all passing through the U-motif and the ATP-binding site residues. Each RyR model structure contained at least one but up to three intra-monomeric branches. Individual branches, which occurred in various proportions in different model structures, differed in specific residues of the ATP-binding site. Branches I4 – I6 also contained residues of the S45 linker, more often in RyR1 than RyR2 isoforms, and more often in the closed pore structures (C, P, I) than in the open structures. Individual structures contained 1 – 3 intra-monomeric branches. Three RyR1 and two RyR2 structures contained only 1 intra-monomeric branch.

The inter-monomeric pathway connecting the EF1/2 loops with the S23* loop was detected by OHM in 5 – 52 % of the first 100 inhibition paths for individual model structures (Table 4, Appendix Table S1). This pathway diverged to 6 branches (I7 – I12), which all involved one of the S23* residues R4736*, D4730*, and I4731* or its hRyR2 equivalent F4660*, identical to those forming a salt bridge or H-bond with the EF-hand region as identified by the PDBePISA data (see above). Notably, this pathway was present in all RyR1 structures except for the RyR1-C but only in one RyR2 structure (Table 4). Individual RyR structures contained 1 – 2 inter-monomeric branches. In the primed and open RyR1 structures, this pathway

490 participated by only 5 – 28 %, but it was dominant by 52% in the inactivated RyR1 structure 7tdg. In the
491 RyR2 open structure 7ua9 it participated by 8% (branch I10). Notably, four out of 6 inter-monomeric
492 branches used the U*-motif: three in RyR1 and one in RyR2 structures. Two branches of the inactivated
493 RyR1 structure 7tdg connected the S23* with the S45* linker directly and not through the U*-motif. The
494 inter-monomeric pathway reached the gate *via* the S6* segment.

Table 4. Fractional occurrence of branches in the inhibition network pathways.

Main branches connecting the INH and GATE sites		Fraction of paths (%)								
		RyR1					RyR2			
		C	P	O	O†	I†	C	C†	O†	O
		7k0t	7tzc	7m6l	7tdh	7tdg	7vmm	7ua5	7ua9	7vmp
Name	Intra-monomeric pathways									
I1	-EF - U - ATP - S6-		42	72	60		100	63		100
I2	-EF - U - ATP - S6-								18	
I3	-EF - U - ATP - S6-								74	
I4	-EF - U - ATP - S45 - S6-		53			48		24		
I5	-EF - U - ATP - S45 - S6-				27					
I6	-EF - U - ATP - S45 - S6-	100			4					
	Subtotal	100	95	72	91	48	100	88#	92	100
	Inter-monomeric pathways									
I7	-EF - S23* - U* - S6*-			14	9					
I8	-EF - S23* - U* - S6*-			14						
I9	-EF - S23* - U* - S6*-		5							
I10	-EF - S23* - U* - S45* - S6*-								8	
I11	-EF- S23*- S45*-S6*-					40				
I12	-EF- S23*- S45*-S6*-					12				
	Subtotal	0	5	28	9	52	0	0	8	0
	TOTAL	100	100	100	100	100	100	88#	100	100

INH and GATE are defined in Table 9. The abbreviations EF, U, ATP, S23, S45, and S6 refer to the EF-hand region, U-motif, ATP-binding site, S23 loop, S45 linker, and S6 helix, respectively. These domains contribute by one or more residues to the path (see Appendix Table S1 for the list of critical residues of individual branches).
† marks a pair of RyR1 and RyR2 structures obtained in the same experiment. # The remaining 12% of the allosteric signal passed through the poorly resolved DR1 region.

495 ## The activation network

496 In the activation network, we defined the Ca^{2+} binding residues of the CD and CTD as the allosteric
497 activation site (ACT), and the hinge and gate residues of the S6 and S6* as the active site (GATE). The
498 active site was the same as defined for the inhibition pathway analysis since no other gates are present
499 in the RyR pore. The large RI values were observed at the ATP-binding site and the C-terminal domain
500 residues near the CFF binding site, in addition to residues contacting ACT and the GATE (Figure 7). In
501 several model structures, RIs larger than the threshold value also occurred at several residues of the S45
502 linker.

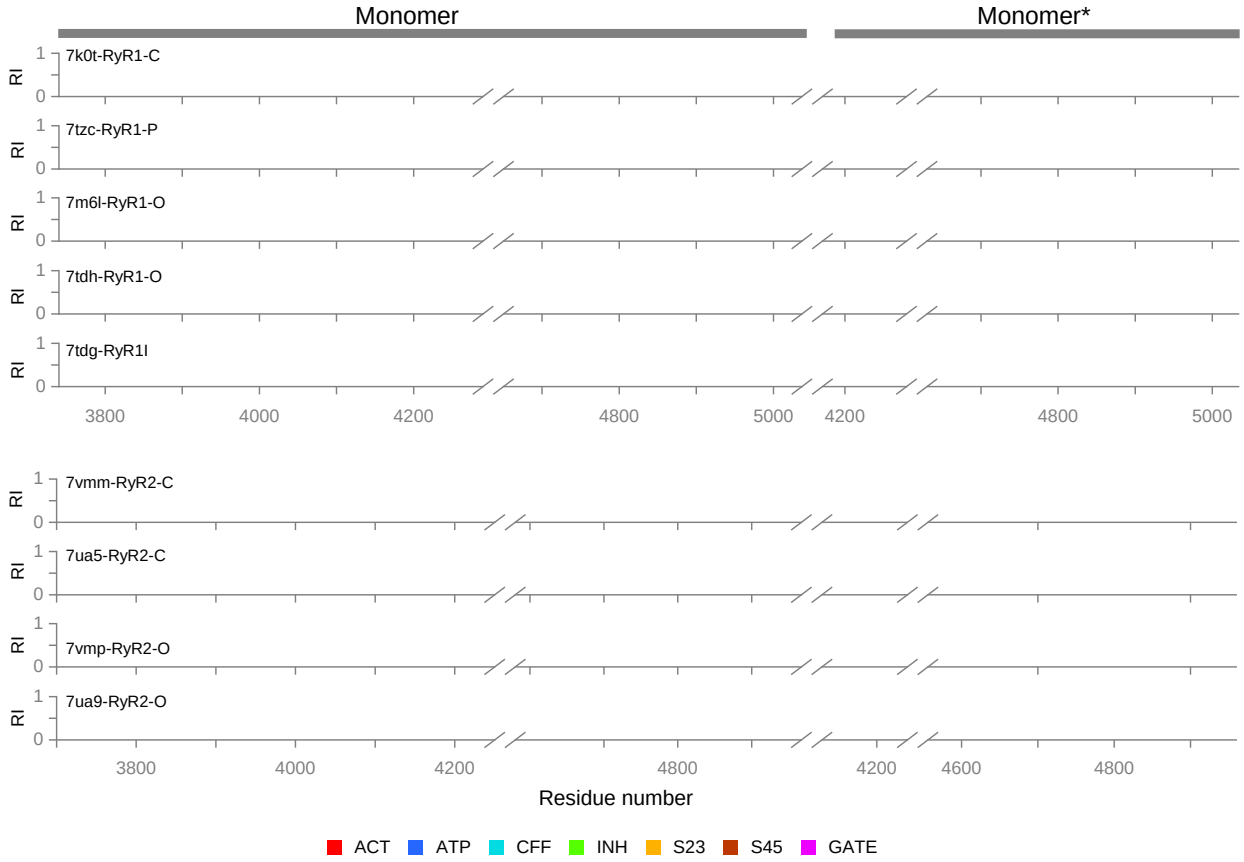

Figure 7. The residue importances in the activation pathways. The RIs were calculated for all detected activation paths and mapped on the RyR sequences. The graph displays only RI > 0.05. The color-coded marks under the sequence axis indicate the positions of important residues from Table 3 and Table 9, see the legend at the bottom: ACT – Ca^{2+}-binding activation site, INH – M^{2+}-binding inhibition site. ATP – ATP-binding site, CFF – caffeine/xanthine binding site, S23 – S23 loop, S45 – S45 linker, GATE – channel gating residues.

The activation network consisted of a single intra-monomeric pathway with nine branches running close to each other (Table 5; Appendix Table S2). All branches comprised the CTD, the U-motif, and the S6 helix. Six branches involved one or more residues of the ATP-binding site, two branches involved residues of the caffeine/xanthine binding site known to support the calcium-dependent activation (des Georges et al., 2016; Chirasani et al., 2022), and three branches involved residues of the S45 linker known to participate in the regulation of channel gating (Murayama et al., 2011; Gomez et al., 2016). Individual model structures contained 1 – 4 branches in various proportions. One RyR1 and one RyR2 structure contained just a single activation branch.

Table 5. Fractional occurrence of branches in the activation network pathway

Main branches connecting the ACT and GATE sites		Fraction of paths (%)								
		RyR1					RyR2			
		C	P	O	O†	I†	C	C†	O†	O
		7k0t	7tzc	7m6l	7tdh	7tdg	7vmm	7ua5	7ua9	7vmp
Name	ATP-site branches									
A1	-CTD – U - ATP - S6-			100		20	100	80		18
A2	-CTD – U - ATP - S6-	60	38						7	21
A3	-CTD – U - ATP - S6-	40								
A4	-CTD – U - ATP - S6-				69					
A5	-CTD - CFF - U - ATP site - S6-									25
A6	-CTD – U - ATP - S45 - S6-					77		20		
	Subtotal	60	38	100	69	97	100	100	7	64
	S45 branches									
A7	-CTD - U - S45 - S6-				14					
A8	-CTD - U - S45 - S6-								93	
	Subtotal	0	0	0	14	0	0	0	93	0
	CFF-site branch									
A9	-CTD - CFF– U - S6-		61		17					36
	Subtotal		61		17					36
	TOTAL	100	99	100	100	97	100	100	100	100

ACT and GATE are defined in Table 9. The abbreviations CTD, U, ATP, CFF, S45, and S6 refer to the Central domain, U-motif, ATP-binding site, CFF-binding site, S45 linker, and S6 helix, respectively, which contribute by one or more residues to the path (see Appendix Table S2 for the list of critical residues of individual branches).

† marks a pair of RyR1 and RyR2 structures obtained in the same experiment.

Interaction between the calcium activation and calcium inhibition networks.

The model RyR structures and their interacting pathways are correlated in Table 6 (the complete list of the critical residues is given in Appendix Table S3). Each of the six intra-monomeric inhibition branches interacts with at least one activation branch. The largest number of interactions occurs in branch I1, which interacts with 4 activation branches in 2 RyR1-O, 1 RyR1-P, 2 RyR2-C, and 1 RyR2-O structures. The smallest number of interactions occurs in branches I2 and I3, which interact only with A2 and only in the RyR2-O structure 7ua9, which does not present other interactions. On the other hand, the activation branch A2 interacts with 3 inhibition branches in 1 RyR1-C, 1 RyR1-P, and 2 RyR2-O structures. Branches I7 – I9 and branch A9 presented no interactions in the allosteric network. A systematic interaction pattern for branches and structures was best revealed when the branches of the networks were connected graphically (Figure 8).

Table 6. Interactions between pathways of the activation and inhibition network.

	A1	A2	A3	A4	A5	A6	A7	A8	A9
I1	RyR1-O 7m6l$ RyR2-C 7vmm$ RyR2-C 7ua5$ RyR2-O 7vmp$	RyR1-P 7tzc RyR2-O 7vmp		RyR1-O 7tdh	RyR2-O 7vmp				
I2		RyR2-O 7ua9							
I3		RyR2-O 7ua9							
I4	RyR1-I 7tdg	RyR1-P 7tzc				RyR1-I 7tdg$ RyR2-C 7ua5$			
I5				RyR1-O 7tdh					
I6		RyR1-C 7k0t	RyR1-C 7k0t	RyR1-O 7tdh			RyR1-O 7tdh$		
I7									
I8									
I9									
I10						RyR1-I 7tdg#			
I11						RyR1-I 7tdg#			
I12								RyR2-O 7ua9$#	

$ marks structures where the same residue of the ATP-binding site or the S45 linker, participates in both the inhibition and activation network.

marks the interaction of the inter-monomeric inhibition pathway with the activation pathway of the anticlockwise-neighboring monomer.

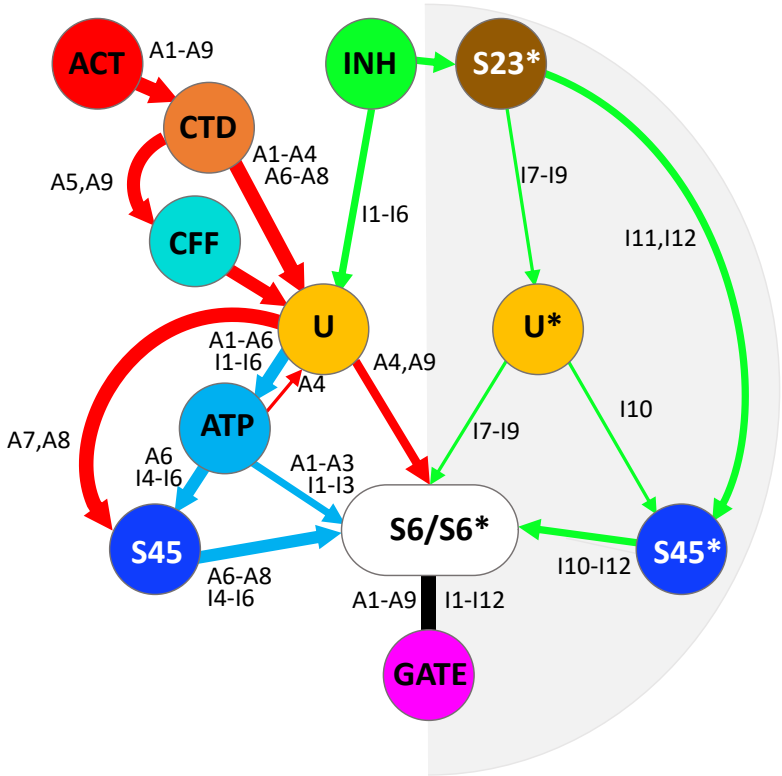

Figure 8. Divalent ion-related allosteric networks of the ryanodine receptor. The scheme integrates the intra-monomeric (white background) and the inter-monomeric pathways (gray background). Note that both pathway types are present in each monomer. Red – the activation network. Green – the inhibition network. Blue – the shared activation and inhibition sub-paths. The branches are labeled in correspondence to Tabs 3 - 5. ACT – the activation site; INH – the inhibition site; CTD – the C-terminal domain; CFF – the caffeine binding site; S23 – the S23 loop; U, U* - the U-motifs; ATP – the ATP binding site; S45, S45* - the S45 linkers; S6/S6* - the S6 helices; GATE - the gating site.

A search for important residues in the allosteric network revealed several residues shared by both networks. Each analyzed RyR structure involved U-motif residues I4218 and F4219 in either the

525 inhibition allosteric network (7tdh, 7tzc, 7ua9), or the activation allosteric network (7tdg and 7k0t), or
526 both (7m6l, 7vmm, 7ua5, 7vmp). In all RyR structures except RyR1-C 7k0t and RyR2-O 7ua9, at least one
527 branch of the allosteric network contained the U-motif residues K4214 and W4205. In all RyR structures
528 except RyR1-C 7k0t and RyR2-O 7ua9, the activation and inhibition branches converged either before or
529 at these U-motif residues, or in the case of 7tdh at the CTD residue Q4947 that follows the U-motif
530 residue F4219 in the pathway. Thus the U-motif residues I4218, F4219, K4214, and W4205 emerge as
531 essential for the allosteric interaction between the activation and inhibition pathways. The residues
532 I4218 and K4214 also participate in the ATP binding site.

533 In all model structures, the majority of activation and inhibition pathways encompassed at least one
534 ATP-binding residue, therefore these pathways may be speculated to affect the affinity of the ATP
535 binding site and regulation of RyR activity by ATP.

536 It should be underlined that the intra-monomeric pathway of the inhibition network interacts with the
537 activation network in all 9 investigated model structures. The U-motif appears central to mixing signals,
538 incoming from the activation and inhibition sites and passing them through the ATP-binding site, and/or
539 S45, or directly to the S6 segment. The S6 segment appears central to the signal integration to control
540 the pore open/closed state in all pathways.

541 5 The allosteric model of the RyR channel operation

542 The assumed *modus operandi* common to RyR channel isoforms across species should consider the
543 single-channel activity as the result of structural transitions. More specifically, under the given
544 experimental conditions the structural states and their allosteric interactions should have counterparts
545 in the functional states and their allosteric transitions. A theoretical model of the ion-dependent RyR
546 operation based on the results of structural analysis should approximate the single-channel data
547 collected at various concentrations of divalent ions. The experimental structural and functional data
548 indicate that:

549 (1) The gate structure of the S6 segment is the only structure that controls the permeation state of the
550 channel pore in both RyR1 and RyR2. This means that both the activation and the inactivation
551 processes act on the same gate. Consequently, the activation and the inactivation are inter-
552 dependent processes.
553 (2) The ion-binding activation site is a self-contained structure composed of equivalent CD and CTD
554 residues in both RyR1 and RyR2. It has a much higher affinity to Ca^{2+} than Mg^{2+} ions, and its allosteric
555 coupling to the channel pore stabilizes the gate in the open state more effectively when occupied by
556 Ca^{2+} than any other ion.
557 (3) The ion-binding inhibition site is formed by the EF1 and EF2 ion-binding loops in both RyR isoforms.
558 It has a similar low affinity to Ca^{2+} and Mg^{2+} ions, and its allosteric coupling to the channel pore
559 stabilizes the gate in the closed position when occupied by either divalent ion. The binding-to-
560 inactivation allosteric coupling efficiency is higher in RyR1 than in RyR2.
561 (4) RyR isoforms adopt mutually congruent structural and functional macrostates. The bound/unbound
562 state of the ligand binding sites defines the state and the structure of the RyR molecule. The

563 equilibrium between macrostates depends on the concentrations and binding constants of
564 ligands/divalent ions.
565 (5) The closed, primed, and inactivated RyR structures have the gate of all 4 monomers in the closed
566 position. The open RyR structure has the gate of all 4 monomers in the open position.
567 (6) The primed state is defined by activators bound to their respective ATP-binding and/or caffeine-
568 binding sites.
569 (7) The ion-dependent allosteric network of RyR consists of the intra- and inter-monomeric pathways.
570 The intra-monomeric activation and inhibition pathways merge at the U-motif near the ATP and CFF
571 binding pockets. The inter-monomeric pathway is a specialized ion-dependent inhibitory path more
572 prominent in RyR1.
573 (8) In the absence of a structure of the inactivated RyR2, the model assumes that such a structure exists
574 at high concentrations of divalent ions and differs from the inactivated RyR1 structure by the extent
575 of EF-hand - S23* coupling.

576 ## Construction of the model of RyR operation

577 The analysis of homotetrameric RyR structures revealed that all four RyR monomers in concord adopt
578 one of four principal structural macrostates – the closed, the primed, the open, and the inactivated. The
579 structure of macrostates depends on the concentrations of divalent ions, ATP, and caffeine. Closed and
580 primed macrostates could be combined into a single closed macrostate of the model since both are
581 closed and cannot be functionally distinguished at a constant ATP concentration. Therefore, we
582 constructed the model of RyR operation, termed the COI (closed-open-inactivated) model, in which we
583 assigned a functional macrostate corresponding to each of the closed/primed, open, and inactivated
584 structural macrostates (Figure 9A). The three macrostates were interconnected so that each could be
585 directly transformed into another since each state was observed at a range of calcium concentrations.
586 As in our previous RyR gating models (Zahradnik et al., 2005; Zahradnikova et al., 2010; Iaparov et al.,
587 2022), transitions between channel states were considered spontaneous, with the unliganded RyR
588 strongly preferring the closed state. A transition between macrostates transpires as a cooperative
589 conformational change of all four monomers that occurs even without ligand binding, albeit with low
590 probability. The binding of ligands changes the relative energies of macrostates, thus also the likelihood
591 of finding the channel in a particular macrostate.

592 The operational schemes in Figure 9 describe transitions between (A) and within (B, C, D) individual
593 macrostates respecting the identified allosteric pathways (A1-A9; I1-I12; Figure 10) as described by Eqs.
594 4. Transitions between the unliganded macrostates: closed (squares), open (circles) and inactivated
595 (hexagons) are illustrated in Panel A. Transitions between binding states of the closed macrostate are
596 presented in Panel B. Since the closed macrostate is the reference state, transitions between binding
597 states do not contain allosteric coefficients in this case. Transitions between binding states of the open
598 macrostate are shown in Panel C. The activation allosteric coefficients f_{Ca} and f_{Mg} specify the effect of
599 divalent ion binding to the Ca^{2+}-activation site on the coupling efficiency of the activation pathway (A1-
600 A9). Transitions between binding states of the inactivated macrostate are displayed in Panel D. The
601 interaction factors h_{CaM} and h_{MgM} quantify the interaction between the activation site and the inhibition
602 site resulting from the existence of common sub-paths in the intra-monomeric network (A1-A6; I1-I6).
603 The classical state diagram of the COI model is explained in Extended View Figure EV1.

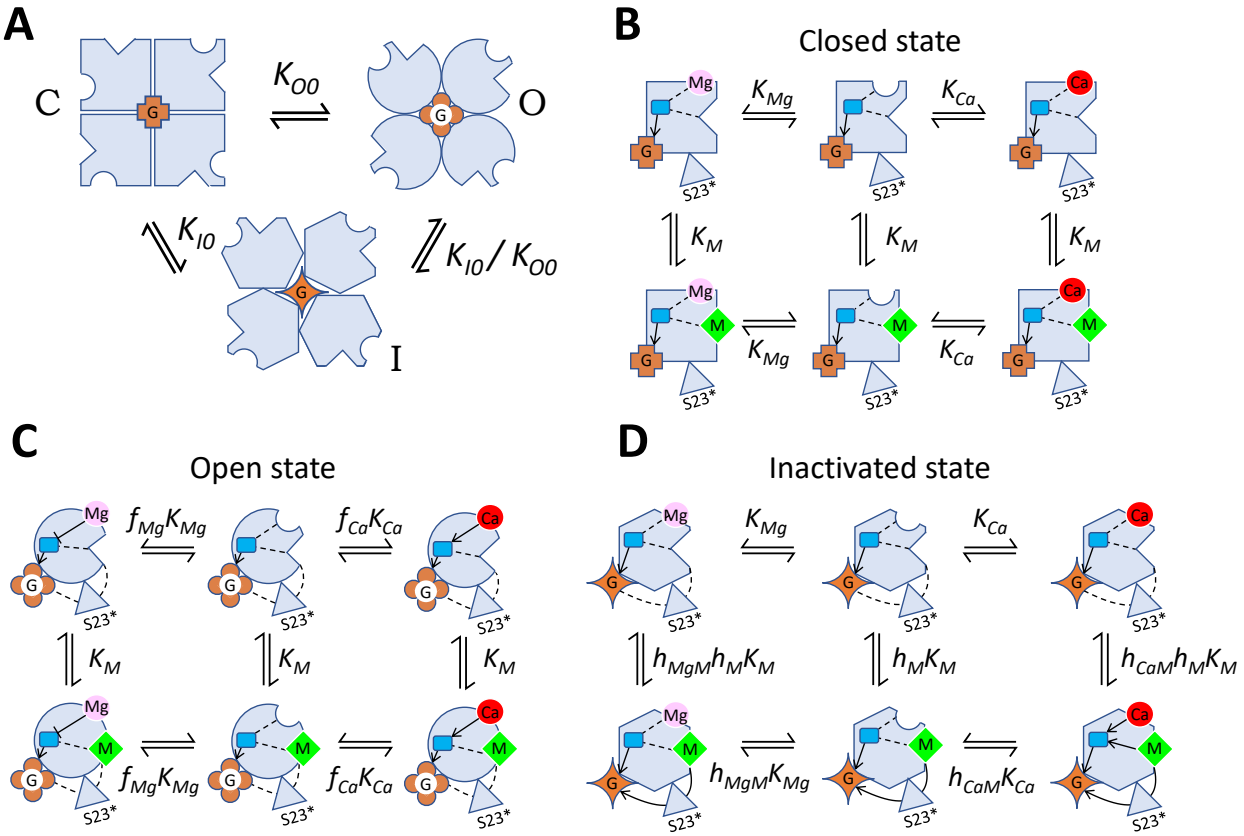

Figure 9. The COI model of RyR channel operation. A: Transitions between the closed, open, and inactivated macrostates of ligand-free RyR. Equilibrium constants of transitions between the respective macrostates are indicated. **B:** The ligand-binding transitions of a monomer in the closed macrostate. **C:** The ligand-binding transitions of a monomer in the open macrostate. **D:** The ligand-binding transitions of a monomer in the inactivated macrostate. **B – D:** Gray shapes represent RyR monomers in the respective macrostates as depicted in A. Equilibrium constants of transitions between the respective states are indicated. Lines and arrows represent the allosteric interaction pathways. Dashed lines - no allosteric regulation. Blunt arrow (⊢) - negative allosteric interaction. The pointed arrows (←) - positive allosteric interaction. Round groove – the activation site. Pointed groove – the inhibition site. Blue square – the interaction site of the activation and the intra-monomeric inhibition pathways (ATP-binding site). Red circles – Ca^{2+}; pink circles – Mg^{2+}; green diamonds – M^{2+} (Ca^{2+} or Mg^{2+}). Brown shapes labeled G - the channel pore with the gate in the closed, open, or inactivated state. The grey triangle represents the S23 loop of a neighboring monomer.

In the equilibrium, the probability of occurrence of a macrostate is given by the respective equilibrium constants and allosteric factors. Allosteric factors multiply equilibrium constants to reflect the changes in the energy of a macrostate relative to the closed macrostate, caused by the binding of an ion. If the affinity of an ion to the new macrostate does not change, the allosteric factor is 1, if the affinity increases the factor is <1; and if the affinity decreases the factor is >1. Transitions between states were characterized in the COI model by allosteric factors of two types – allosteric coefficients and interaction factors. The allosteric coefficients define the binding affinity of a single ligand to the O and I macrostates relative to the ligand's affinity in the closed macrostate. The allosteric coefficients of Ca^{2+} and Mg^{2+} binding at the activation site are defined as f_{Ca} and f_{Mg} in the open macrostate, and h_{Ca} and h_{Mg} in the inactivated macrostate. The inhibition site does not discriminate between Ca^{2+} and Mg^{2+}, therefore the allosteric coefficient is defined as f_M in the open macrostate and h_M in the inhibited macrostate. The interaction factors reflect the changes of ion affinity induced by the simultaneous occupation of both

the activation and inhibition sites and are defined as g_{CaM} and g_{MgM} in the closed macrostate, f_{CaM} and f_{MgM} in the open macrostate, and h_{CaM} and h_{MgM} in the inactivated macrostate.

Since both the activation pathway and the intra-monomeric inhibition pathway lead through the binding site for ATP, the values of f_{Ca}, f_{Mg}, h_{CaM}, and h_{MgM} should depend on the binding of ATP; however, since only the absence of ATP or a single concentration of ATP was considered here, its effect was convolved into the respective allosteric factors, which were allowed to depend on the presence of ATP. To reduce the number of parameters (see above), the interaction between the activation and inhibition binding sites in the COI model was constrained only to the inhibited macrostate, as depicted in Figure 9 D.

The inactivation allosteric coefficient h_M specifies the impact of divalent ion binding to the RyR inhibition site on the gating site, transmitted through the S23* loop of the neighbor monomer. Since the inter-monomeric inhibition pathway does not involve any ATP-binding residues, the value of h_M is independent of the presence of ATP at either monomer.

Derivation of the model open probability equation

In the COI model, the equilibrium probability of the open state, P_O, can be described by Eq. 2, using the approach of statistical mechanics (Marzen et al., 2013):

$$P_O = \frac{\frac{1}{K_{O0}} w_O^4}{\frac{1}{K_{O0}} w_O^4 + w_C^4 + \frac{1}{K_{I0}} w_I^4}, \qquad \text{(Eq. 2)}$$

where w_O, w_C, and w_I are the statistical weights of the open, closed, and inactivated macrostates, respectively; the exponent 4 reflects the cooperative action of 4 monomers, and K_{O0} and K_{I0} are the equilibrium constants of the open and the inhibited ligand-free macrostate, respectively.

Changes in RyR macrostates induced by the binding of ions are expressed through the dependences of w_O, w_C, and w_I on the ion-binding equilibria. The weight factors of the resulting COI model, calculated according to Marzen et al. (2013) and Horrigan and Aldrich (Horrigan and Aldrich, 2002), are then given by:

$$w_C = 1 + \frac{[Ca]}{K_{Ca}} + \frac{[Mg]}{K_{Mg}} + \frac{[M]}{K_M} + \frac{[Ca][M]}{g_{CaM} K_{Ca} K_M} + \frac{[Mg][M]}{g_{MgM} K_{Mg} K_M}, \qquad \text{(Eq. 3A)}$$

$$w_O = 1 + \frac{[Ca]}{f_{Ca} K_{Ca}} + \frac{[Mg]}{f_{Mg} K_{Mg}} + \frac{[M]}{f_M K_M} + \frac{[Ca][M]}{f_{CaM} f_{Ca} K_{Ca} K_M} + \frac{[Mg][M]}{f_{MgM} f_{Mg} K_{Mg} K_M}, \qquad \text{(Eq. 3B)}$$

$$w_I = 1 + \frac{[Ca]}{h_{Ca} K_{Ca}} + \frac{[Mg]}{h_{Mg} K_{Mg}} + \frac{[M]}{h_M K_M} + \frac{[Ca][M]}{h_{CaM} h_M K_{Ca} K_M} + \frac{[Mg][M]}{h_{MgM} h_M K_{Mg} K_M}, \qquad \text{(Eq. 3C)}$$

where the square brackets stay for the concentration of an ion in mol.l^{-1}, and [M] = [Ca] + [Mg] stays for the concentration of divalent ions M. The individual terms at the right side of the equations characterize individual ion-binding state transitions of a monomer in the closed, open, and inactivated macrostates.

Equation 2 contains two constants and three independent variables, which are described in Eqs. 3 by three variables (two independent concentrations of Ca^{2+} and Mg^{2+}, and their sum M^{2+}) and 15 parameters characterizing the chemical equilibria. The single-channel data in the literature consist of

concentration dependencies of open probability under different experimental conditions that do not always cover the full range and often display relatively large errors of measurement. This data paucity together with the relatively simple and similar shapes of ion-dependencies (see Figure 10) does not allow direct determination of all 17 parameters per concentration dependence by fitting Eqs. 2 and 3 to data points due to the parameter redundancy problem. Since solving this problem experimentally is not practical or even feasible, we resolved it by a substantial reduction of the number of parameters in Eqs. 3A-C, while respecting the observed allosteric pathways. We used the following practical assumptions: The allosteric effect of Ca^{2+} and Mg^{2+} bound at the activation site occurs only in the open macrostate, meaning that the values of h_{Ca} and h_{Mg} in Eq. 3C can be set to 1, i.e., the allosteric effect of ion binding to the activation site on the inactivated macrostate can be considered negligible. Similarly, the allosteric effect of M^{2+} bound at the inhibition site occurs only in the inactivated macrostate, i.e., f_M in Eq. 3B can be set to 1. Finally, the interaction between the activation and the inhibition site occurs only in the inactivated macrostate, i.e., the values of interaction factors f_{CaM}, g_{CaM}, f_{MgM}, and g_{MgM} in Eqs. 3A and B can be set to 1. By applying these suppositions the Eqs. 3A-C can be simplified to Eqs. 4A-C that contain only 8 independent parameters:

$$w_C = 1 + \frac{[Ca]}{K_{Ca}} + \frac{[Mg]}{K_{Mg}} + \frac{[M]}{K_M} + \frac{[Ca][M]}{K_{Ca}K_M} + \frac{[Mg][M]}{K_{Mg}K_M}, \qquad \text{(Eq. 4A)}$$

$$w_O = 1 + \frac{[Ca]}{f_{Ca}K_{Ca}} + \frac{[Mg]}{f_{Mg}K_{Mg}} + \frac{[M]}{K_M} + \frac{[Ca][M]}{f_{Ca}K_{Ca}K_M} + \frac{[Mg][M]}{f_{Mg}K_{Mg}K_M}, \qquad \text{(Eq. 4B)}$$

$$w_I = 1 + \frac{[Ca]}{K_{Ca}} + \frac{[Mg]}{K_{Mg}} + \frac{[M]}{h_M K_M} + \frac{[Ca][M]}{h_{CaM}h_M K_{Ca}K_M} + \frac{[Mg][M]}{h_{MgM}h_M K_{Mg}K_M}, \qquad \text{(Eq. 4C)}$$

i.e., together with Eq. 2, we remained with only 10 independent parameters (see the list in Table 7).

6 Description of RyR operation by the COI model

The published single-channel data on Ca^{2+} and Mg^{2+} dependence of the open probability of RyR1 and RyR2 are quite limited by the range, completeness, and compatibility of experimental conditions. The experimental data for validation of the model were taken from experiments of Fill et al. (1991), Chu et al. (1993), Zahradnikova et al. (2003), Tencerova et al. (2012), and Li et al. (2013) that conformed with conditions used for collecting RyR molecules for cryo-electron microscopy determination of their structure. These include isolated cardiac microsomal vesicles incorporated into lipid bilayers either under near-physiological conditions with a total ATP concentration of 2 - 3 mM, free Mg^{2+} in the range of 0 - 1.3 mM, and free Ca^{2+} in the range of 0.1 – 100 µM at the cytosolic side and 0.1 - 1 mM at the luminal side (rat or canine cardiac microsomes (Zahradnikova et al., 2003; Tencerova et al., 2012; Li et al., 2013)) or under simpler conditions in the absence of Mg^{2+} and ATP, at free cytosolic Ca^{2+} in the range of 0.1 – 4000 µM and approximately 10 µM luminal Ca^{2+} (canine cardiac microsomes and rabbit or human skeletal muscle microsomes (Fill et al., 1991; Chu et al., 1993)).

The whole experimental dataset consists of 8 functional relations with 54 data points represented by the mean and the standard error of the mean (Figure 10), obtained under five different experimental conditions that did not cover the full range and often displayed relatively large errors of measurement. If fitted separately, they would need 64 separate parameter values. Therefore, to reduce the number of

684 parameter values, we combined published data into three groups by neglecting the differences in RyR
685 single-channel activity between species (Table 7, and Figure 10 A, B, C). We combined data obtained in
686 rat (Tencerova et al., 2012; Li et al., 2013) and canine (Zahradnikova et al., 2003) RyR2 channels in the
687 presence of ATP, luminal Ca^{2+}, and at various cytosolic Ca^{2+} and Mg^{2+} levels, to estimate the parameter
688 values of RyR2 transitions at near-physiological conditions (Table 7, "RyR2 + ATP" group). The data from
689 canine RyR2 (Chu et al., 1993) in the absence of Mg^{2+} and ATP and at a low level of luminal Ca^{2+} formed
690 the group "RyR2 − ATP" (Table 7). We combined human (Fill et al., 1991) and rabbit (Chu et al., 1993)
691 RyR1 in the absence of Mg^{2+} and ATP and at a low level of luminal Ca^{2+} (Table 7, "RyR1 − ATP" group).
692 The groups "RyR1 − ATP" and "RyR2 − ATP" allowed us to characterize the difference between RyR1 and
693 RyR2 channels. The groups "RyR2 + ATP" and "RyR2 − ATP" allowed us to characterize the effect of ATP
694 on RyR2. This procedure led to the reduction of the number of parameter values to 24 for the whole
695 system of equations approximating the three data groups (Table 7).

Table 7. The best-fit parameter values of the COI model (Equation 4).

Parameter	Description	RyR2 + ATP	RyR2 − ATP	RyR1 − ATP	Reference or justification
K_{O0}	Equilibrium constant for the transition C ↔ O (Eq. 2)	**10 800**			Taken from (Zahradnik et al., 2005)
K_{I0}	Equilibrium constant for the transition C ↔ I (Eq. 4)	**10 800**			Set equal to K_{O0}
K_{Ca} (μM)	Dissociation constant of Ca^{2+} from the activation site (Eq. 4)	0.59 ± 0.15			Best fit value
K_{Mg} (μM)	Dissociation constant of Mg^{2+} from the activation site (Eq. 4)	36.3 ± 4.3			Best fit value
K_M (μM)	Dissociation constant of Mg^{2+} from the inhibition site (Eq. 4)	**546**			Taken from (Iaparov et al., 2022)
f_{Mg}	Allosteric factor of Mg^{2+} at the activation site (Eq. 4)	**3.25**			Taken from (Iaparov et al., 2022)
f_{Ca}	Allosteric factor of Ca^{2+} at the activation site (Eq. 4)	0.029 ± 0.005	0.10 ± 0.003	0.15 ± 0.01	Best fit values
h_M	Allosteric factor of M^{2+} at the inhibition site (Eq. 4)	**1**	**1**	0.28 ± 0.10	See text
h_{CaM}	Interaction factor between Ca^{2+} at the activation site and M^{2+} at the inhibition site (Eq. 4)	0.016 ± 0.003	0.11 ± 0.04		Best fit value
h_{MgM}	Interaction factor between Mg^{2+} at the activation site and M^{2+} at the inhibition site (Eq. 4)	**1**	**1**	**1**	See text
$h_M.h_{CaM}$		*0.016 ± 0.003*	*0.11 ± 0.04*	*0.031 ± 0.11*	*assuming normal distribution*
COD	Coefficient of determination	0.953			

Values in bold were fixed in all calculations. Values presented as the mean ± error represent the best-fit values and the standard error of the fit. Parameters in the column "RyR2 + ATP" correspond to fits to the black and green data points in Figure 10 A and B. Parameters in columns "RyR2 − ATP" correspond to fits to the black data points in Figure 10 C. Parameters in columns and "RyR1 − ATP" correspond to fits to the blue and red data points in Figure 10 C.

696 The algorithm used for fitting (see Methods) provided detailed information on the quality of fit,
697 including thorough control of the fitting process and a detailed description of the fitting results, namely,
698 the standard error of the fit, parameter dependency, and statistical significance of the estimated
699 parameter value. This allowed us to solve the anticipated problems of convergence and over-
700 parametrization by fixation of parameter values with the highest dependency and sharing parameter
701 values between groups when they were not significantly different from each other.

702 In the first step, we fixed several parameters at previously published values or considered an *a priori*
703 estimate (see Table 7). The value of K_{O0} was set at the value estimated in our previous study based on a
704 principally similar allosteric gating model of RyR2, where its determination was enabled by the existence
705 of data for the open probability of RyR channels with a variable number of calcium activation-deficient
706 monomers (Zahradnik et al., 2005). The K_{O0} value was set the same for all three data groups, based on
707 the structural similarity of RyR1 and RyR2 in the closed state. The stability constant of the unoccupied
708 inactivated state (K_{I0}) was *a priori* considered equal to that of the unoccupied open state (K_{O0}) since we
709 consider both the open and the inactivated macrostate in the absence of ligands thermodynamically
710 equal.

711 The values of f_{Mg} and K_M were set in all three groups at their values estimated in our previous study on
712 RyR2 channels based on fitting of the open probability, open times, and the rate of activation by a
713 kinetic model of allosteric gating, see (Iaparov et al., 2022). The equivalence of f_{Mg} in RyR1 and RyR2 was
714 based on the identical structure of the activation site in both isoforms. The equivalence of K_M in RyR1
715 and RyR2 was based on the similar values of the ion-binding parameters of the EF-hands in RyR1 and
716 RyR2 estimated in the section "The propensity of EF1 and EF2 loops to bind divalent ions". The ion
717 dissociation constants K_{Ca} and K_{Mg} were shared between all data groups since the structure of the
718 activation site in both isoforms is identical.

719 The parameter defining the strength of allosteric interaction between the Mg^{2+} bound at the activation
720 binding site and M^{2+} bound at the inhibition binding site (h_{MgM}) could not be optimized for any isoform,
721 due to the absence of Po data in the presence of Mg^{2+} for RyR1 channels. The test of h_{MgM} variation for
722 RyR2 between 1 and 0.2 yielded a negligible impact on χ^2 (5%) and coefficient of determination (0.3%)
723 and did not affect significantly the remaining parameter values. Therefore, h_{MgM} was set to 1 for all three
724 group. This solution practically disconnected Mg^{2+} binding to the activation site from the intra-
725 monomeric inhibition pathway.

726 The value of parameter h_M, which defines the strength of the allosteric effect of M^{2+} bound at the
727 inhibition site on the inter-monomeric pathway, was set to 1 for RyR2 data (groups "RyR2 + ATP" and
728 "RyR2 − ATP"), in correspondence to the small intensity of the inter-monomeric pathway in the RyR2
729 isoform (Table 4). The effect of this simplification was tested by varying h_M of RyR2 in the interval $0.25 \leq$
730 $h_M \leq 1$, which returned negligible impact on χ^2 (4%) and coefficient of determination (0.2%), a
731 proportional change in h_M for RyR1 data, a reciprocal change in h_{CaM} of both RyR1 and RyR2, and
732 undetectable change in the remaining parameter values. This interdependence means that the dataset
733 does not allow the determination of the unequivocal values of h_M and h_{CaM} but only of their product
734 $h_M.h_{CaM}$ (Table 7, bottom line). The parameters h_{CaM} for the data groups "RyR2 − ATP" and "RyR1 − ATP",
735 if optimized as independent parameters, were not significantly different from each other but the

736 parameter values of h_M and h_{CaM} were highly correlated and their standard errors of the fit were large;
737 therefore, the parameter h_{CaM} was shared for both "RyR2 − ATP" and "RyR1 − ATP" data groups in the
738 final optimization. In the end, eight parameters of the COI model were set free for fitting the
739 experimental data, as summarized in Table 7. It should be noted that the minimization criterion was the
740 minimal chi-square value for the whole dataset.

741 The solutions of the COI model for the dependences of the RyR1 and RyR2 open probabilities on
742 concentrations of Ca^{2+} and Mg^{2+} ions (Figure 10, lines; Table 7, parameter values) indicate that the
743 model complies satisfactorily with the data obtained at a wide range of conditions. These include four
744 species, two RyR isoforms, and the presence or absence of cytosolic ATP, Mg^{2+}, and luminal Ca^{2+} ions.

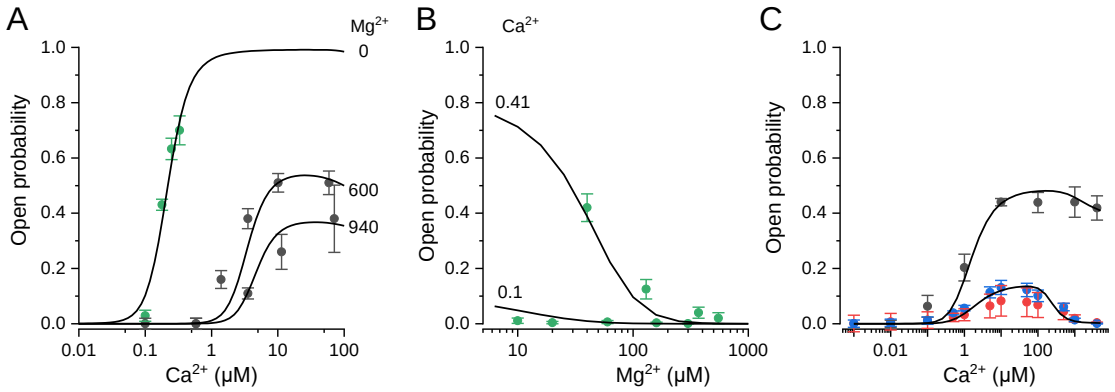

Figure 10. Description of RyR open probability data by the COI model of RyR operation. The data points represent the mean and SEM of the single-channel open probability values read from the referenced publications (see below). The curves represent the theoretical predictions of the COI model (Eqs. 4) with the corresponding parameters for individual data groups in Table 7. **A** – Calcium dependence of the single-channel P_O at cytosolic [Mg^{2+}] of 0, 600, and 940 µM (indicated next to the data) in the presence of 3 mM cytosolic ATP and 1 mM luminal Ca^{2+}. Black points – canine RyR2 channels (Zahradnikova et al., 2003). Green points - rat RyR2 channels (Tencerova et al., 2012). Lines - theoretical predictions of the COI model with parameters for the "RyR2 + ATP" group in Table 7. **B** – Magnesium dependence of the single-channel P_O at cytosolic [Ca^{2+}] of 0.1 and 0.41 µM (indicated next to the data) in the presence of 3 mM cytosolic ATP and 1 mM luminal Ca^{2+}. Green points - rat RyR2 channels (Tencerova et al., 2012; Li et al., 2013). Lines - theoretical predictions of the COI model with parameters for the "RyR2 + ATP" group in Table 7. **C** – Calcium dependence of the single-channel open probability obtained in the absence of cytosolic ATP and Mg^{2+} and with 10 µM luminal Ca^{2+} (Fill et al., 1991; Chu et al., 1993). Black points - canine RyR2 channels (Chu et al., 1993). Blue points - human RyR1 channels (Fill et al., 1991). Red points – rabbit RyR1 channels (Chu et al., 1993). Lines - theoretical predictions of the COI model with parameters for the "RyR1 − ATP" or "RyR2 − ATP" groups in Table 7.
It should be noted that only f_{Ca} and h_M were allowed to vary with the isoform of RyR, while f_{Ca} and h_{CaM} were allowed to vary with the presence of ATP, see their best-fit values in Table 7. All equilibrium constants (K_{O0}, K_{Ca}, K_{Mg}, K_{I0}, K_M) had common values for the whole dataset (Table 7).

745 As mentioned above, the allosteric inhibition factor h_M was fixed to 1 for fitting RyR2 data; this means
746 that the inter-monomeric inhibition pathway was made independent of the occupation of the inhibition
747 site by M^{2+}. Still, however, the intra-monomeric inhibition pathway is operational and RyR2 inactivation
748 is thus controlled by the interaction factor h_{CaM}, which affects the open probability when the activation
749 site is occupied by Ca^{2+} and the inhibition site is occupied by Ca^{2+} or Mg^{2+} (Figure 9 D). In other words,
750 the simultaneous occupation of both the activation and the inhibition site by divalent ions makes the
751 inhibited macrostate energetically more favorable also in RyR2. Therefore, due to the interaction of the
752 intra-monomeric inhibition pathway with the activation pathway, the reduction of P_O can occur even

753 without the recruitment of the inter-monomeric pathway; the strength of this interaction, h_{CaM},
754 determines the sensitivity to inhibition by divalent ions in both RyR isomers.

755 The analysis of inactivation parameters of RyR1 and RyR2 (Table 7) shows that in the absence of ATP, the
756 overall inactivation (proportional to $1/(h_M.h_{CaM})$) is 3.5× more effective in RyR1 than in RyR2 (0.11/0.031
757 = 3.5). In the presence of ATP and luminal Ca^{2+}, the inactivation of RyR2 is about 7× more effective than
758 in the absence of ATP (0.11/0.016) = 6.9). The relative efficacy of inactivation in RyR1 and RyR2 as well
759 as in the absence and presence of ATP were not affected by the h_M value set for RyR2. However, this
760 value strongly affected the predicted efficacy of the inter-monomeric inhibition pathway relative to the
761 intra-monomeric one. The relative importance of the inter-monomeric pathway increased with inverse
762 proportion to the square of the set value of h_M.

763 In the COI model, the Ca^{2+} and Mg^{2+} dissociation constants of the activation site (K_{Ca}, K_{Mg}, Table 7) as
764 well as the M^{2+} dissociation constant of the inhibition site (K_M, Table 7) are the same for RyR1 and RyR2
765 independent of the species. Independent of the species is also the allosteric factor f_{Ca} controlling the
766 maximum open probability and the apparent sensitivity to activation by Ca^{2+}; however, it is significantly
767 different in RyR1 and RyR2 as well as in the absence and presence of ATP in the case of RyR2 (Table 7).
768 Moreover, the interaction factor h_{CaM} is independent of the species and the RyR isoform in the absence
769 of ATP, and it is the same for RyR2 in both species in the presence of ATP. In this sense, the COI model
770 unifies the published single-channel data on RyR activity, which appeared inconsistent among isoforms,
771 species, and experimental conditions.

Discussion

To elucidate the mechanism of RyR operation, we compared the structures and the activity profiles of RyR1 and RyR2 channels at a range of cytosolic Ca^{2+} and Mg^{2+} concentrations. Examination of the EF-hand region as a candidate divalent ion-binding inhibition site in RyR1 and RyR2 structures indicated that in both isoforms the EF1 and EF2 have a similar predisposition to bind M^{2+}; thus the difference between RyR isoforms in the propensity to inactivation by divalent ions should reside in the transmissibility of the M^{2+} binding signal from the inhibition site to the channel gate. Structural analysis of 26 RyR1 and 17 RyR2 structures revealed a single major difference in the configuration of RyR1 and RyR2 domains that resided in the orientation of the EF-hand relative to the S23 loop of a neighbor monomer (Figures 4 and 5). Other domains in the core RyR structures differed in their positions in the closed state relative to that in the open, primed, or inactivated states; nevertheless, they were similar in RyR1 and RyR2. These facts allow us to conclude that the EF1 and EF2 loops represent the inhibitory M^{2+} binding site in both RyR isoforms since they bind divalent ions well, and the interaction between the EF-hand region and the S23 loop is stronger in RyR1 than in RyR2. Thus, the difference in the inactivation of RyR1 and RyR2 by M^{2+} appears to be explainable simply by the different electrostatic interactions of their EF-hands with the S23* loops specific for RyR isoforms.

The situation turned even more interesting in the analysis of the allosteric network between the divalent ion-binding inhibition site and the gate and between the Ca^{2+}-binding activation site and the gate. This revealed two major pathways in the core structure of both RyR isoforms. The robust intra-monomeric pathway that shares the inhibition and the activation branches and involves residues of the U-motif near and including the ATP- and caffeine-binding sites was present in each of the closed, open, primed, and inactivated structural states. The less robust inter-monomeric pathway, present in all open, primed, and inactivated structural states of RyR1 and one open state of RyR2, uses the connection between the EF-hand region and the S23 loop of neighbor monomers. Both pathways may spread the inhibition signal to the common channel gate at the S6 helix either directly from the U-motif or via the S45 linker (Figure 8).

The question of how this complex structure may fulfill the RyR function was approached by mathematical modeling. We built an operational model based on structural data and applied it to the set of published single-channel data on the RyR channel open probability, measured under similar near-physiological conditions as the analyzed RyR structures. The operation model was built on the premise of the correspondence between structural and functional macrostates. We postulated the COI model with the closed, open, and inactivated, mutually connected macrostates, and with relative occupancy of the macrostates controlled by ion-binding equilibria among them. The primed state was not resolved from the closed macrostate. Each macrostate has the activation and inhibition divalent ion binding sites and reaction paths obeying the major allosteric pathways. The probability of the COI model reaching the open macrostate depends on the concentration of divalent ions, their respective binding constants, and four allosteric coefficients that regulate the transitions between the channel states. The values of model parameters were found by approximating the experimental dataset of 54 open probabilities from four laboratories, determined at a broad range of Ca^{2+} and Mg^{2+} concentrations, in RyRs isolated from skeletal and cardiac muscles of various mammals. We considered the interspecies differences negligible for simplification. This allowed us to combine the data into three groups with the number of data points

allowing the approximating algorithms to converge to acceptable solutions. After the optimization of the parameter set, the COI model simulation provided reasonable correspondence to experimental data points.

The basic features of the COI model, common to RyR1 and RyR2, are the activation site with a high affinity for Ca^{2+} and a low affinity for Mg^{2+} and the inhibition site with a low affinity for both Ca^{2+} and Mg^{2+}. The difference is in the values of some allosteric parameters that were dependent on either the RyR isoform or the presence/absence of ATP. The allosteric strength of Ca^{2+} binding to the activation site for opening the gate was higher in RyR2 than in RyR1; the allosteric strength for closing the gate by M^{2+} binding to the inhibition site was higher in RyR1 than in RyR2; but the interaction between the inhibition and activation sites was identical in RyR1 and RyR2. The presence of ATP and luminal calcium transpires as the increase in both the activation strength of Ca^{2+} and the interaction strength between the inhibition and the activation site.

Comparison with previous studies

This is the first study that addresses structural relationships related to divalent ion control of RyRs using a large set of structures. Previously, many authors made illuminating discoveries based primarily on a limited set of structures (Bai et al., 2016; Chi et al., 2019; Iyer et al., 2020; Kobayashi et al., 2022) or using one structure for each RyR state (Chirasani et al., 2022; Nayak and Samso, 2022). Our approach based on the analysis of a collection of compatible structures allowed generalization of the partial results on the RyR structure and revealed the interaction of allosteric pathways.

The importance of the U-motif residues I4218 and F4219, which we observed in the allosteric networks of most RyR1 and RyR2 model structures is underlined by the finding that the corresponding RyR2 residues I4172 and F4173 were found important for the interaction of the U-motif with the C-terminal domain and S6 helix, respectively (Kobayashi et al., 2022), and their alanine substitution led to the gain of function for RyR2 (Murayama et al., 2011).

Greene et al. (2022) observed in molecular dynamics simulations that the S45 linker of all monomers has to assume the “open” position for the channel to be open, suggesting their intimate involvement with the transitions between macrostates. The residues T4825, I4826, S4828, and S4829, present in several branches of the activation and inhibition networks, were shown to be involved in RyR1 gating (Murayama et al., 2011), and the mutation T4825I was shown to weaken RyR1 inhibition by Ca^{2+} (Gomez et al., 2016). The existence of the inter-monomeric inhibition pathway in the open RyR2 structure 7ua9 and the presence of the functionally important S45 residues corresponding to rRyR1 T4825, I4826, S4828, and S4829 in its allosteric network suggests that the RyR2 channels might potentially be inactivated also through the inter-monomeric pathway. This is in agreement with the satisfactory fit of RyR2 data with h_M reduced to 0.25. Uehara et al. (2017) found that K4821 of S45 is a critical residue at which cytosolic and luminal inputs converge. We have observed this residue both in the activation and inhibition allosteric pathways of the inhibited RyR1 model structure 7tdg and the closed RyR2 structure 7ua5 and the inhibition pathways of three other RyR1 model structures (Appendix Tables S1, S2). The determination of the role of luminal Ca^{2+} in RyR gating deserves further study, considering the crucial role of the highly dynamic Ca^{2+} content of SR cisternae (Kubalova et al., 2005; Ziman et al., 2010).

852 To date, allosteric pathways in ryanodine receptors have been examined only in one study (Chirasani et
853 al., 2022). These authors analyzed activation pathways in the closed 5t15, primed 5tap, and open 5tal
854 RyR1 structures (des Georges et al., 2016) and identified allosteric pathways common for the Ca-, ATP-,
855 and caffeine-binding sites. Our results can be compared to those of Chirasani et al. (2022) only partially
856 since we have not included the structures analyzed by Chirasani et al. (2022) in our analysis due to their
857 lower resolution than the later structures 7m6l and 7tzc (Melville et al., 2022a; Melville et al., 2022b). In
858 the RyR1-C structure 5t15 (des Georges et al., 2016), Chirasani et al. (2022) identified in the Ca-
859 activation network several residues that we identified in the RyR1-C structure 7k0t (Nayak and Samso,
860 2022): the CTD residue Y4994, the U-motif residue F4217, and the S6 segment residues Q4946 and
861 E4942. The ATP-binding residue I4218 present in the activation pathway of 7k0t occurred only in a less
862 important pathway of 5t15. The incomplete residue conformity in allosteric pathways may be caused by
863 the occupation of the ATP-binding site by ACP in the structure 7k0t, and the empty ATP-binding site in
864 5t15. In the case of the open RyR1 structures, Chirasani et al. (2022) observed in the Ca activation
865 pathway of 5tal (des Georges et al., 2016) the important ATP-binding residues K4214 and I4218, the CTD
866 residues K4998 and Y4994, and the S6 segment residues Q4946, E4942, and D4938 leading to the gate
867 as we observed in the structure 7m6l (Melville et al., 2022b). The subtle differences between our and
868 the Chirasani's et al. (2022) study might be either due to the differences in the experimental conditions
869 (concentrations of TCEP, ACP vs. ATP, ionic strength) and the limited resolution of the older structures
870 (des Georges et al., 2016).

871 Chirasani et al. (2024) reported a significant increase of IC50 for ^{3}H-ryanodine binding (RyR inhibition)
872 by Ca^{2+} (from ≈0.8 to ≈2.5 mM) and Mg^{2+} (from ≈1.2 to ≈4.5 mM) upon introducing the mutation K4101D
873 into the EF-hand region of RyR1. Mutations K4101A and K4101M also had a significant but smaller
874 effect. On the other hand, mutations of the hydrogen-bonding partner of K4101 in the S23* loop to
875 D4730K or D4730N did not affect RyR inactivation. In the light of our allosteric pathway analysis, these
876 results can be explained by the transmission of the allosteric signal from K4101 not only to D4730 but
877 also to I4731 (Figure 5B, Appendix Table S1). Thus the mutation of only D4730 is not sufficient to block
878 the allosteric transmission through these domains. Interestingly, however, the K4101E mutation had an
879 unexpected effect: in addition to increased IC50 it also increased the EC50 for Ca^{2+}-dependent activation
880 of ^{3}H-ryanodine binding (Chirasani et al., 2024), difficult to explain by current data.

881 Based on their structural analysis of the open RyR1 structure 5tal, Chirasani et al. (2024) proposed that
882 the narrow gap between the EF hand domain and S23* loop of RyR1, necessary for H-bonding
883 interactions between these two domains, is a consequence of the binding of Ca^{2+} to the EF-hands.
884 However, our structural and bioinformatics analysis (Figures 2 and 3) revealed a similar potential for
885 interaction between the EF-hand region and the S23* loop not only in the inactivated but also in the
886 open and primed RyR1 structures at intermediate calcium concentrations. The presence of EF hand-S23*
887 hydrogen bonds in all RyR1 structures suggests that the proximity of the EF hand domain and S23* loop
888 is a structural trait distinguishing RyR1 from RyR2, not a consequence of Ca^{2+} binding to the EF hand.

889 The recent RyR1 structure 7umz (Nayak et al., 2024) demonstrated binding of Mg^{2+} ion in the activation
890 site, confirming thus the functional studies that established competition between Ca^{2+} and Mg^{2+} at the
891 RyR activation site (Laver et al., 1997; Zahradnikova et al., 2003; Zahradnikova et al., 2010). This
892 structure, although obtained in the presence of 10 mM Mg^{2+}, was defined as the closed state, since the

structure of the activation site resembled that in the absence of bound Ca^{2+} despite the presence of a bound Mg^{2+} ion (Nayak et al., 2024). However, the low flexion angle (-2.8°) and the configuration of the EF-hand region relative to the S23* loop reported by Nayak et al. (Nayak et al., 2024), as well as their distance (Figure 2, magenta) and the number of interactions (Figure 3, magenta) compared in this work, resemble more the primed and the inactivated state than the closed state. However, the position of the EF-hand region relative to the Central domain differs from RyR1 in both the closed and the Ca^{2+}-inactivated states (Figure 4, magenta), similarly as in RyR2 structures. This peculiar conformation can be speculated to result from the independence of the functional macrostate (closed/primed – open – inactivated) from the occupation status of the monomer binding sites, as postulated in the MWC theorem (Monod et al., 1965) and embedded in the COI model. The parameters of the COI model for RyR1 channels in the absence of ATP (Table 7) predict the channel to reside predominantly in the closed state. However, variation of h_{MgM} in the interval between 1 and 0.2, which was shown to be acceptable for RyR2 channels, results in a progressive shift towards the inactivated state (from <1% at h_{MgM} = 1 to ≈80% at h_{MgM} = 0.2). Thus, distinguishing the state of the channel at 10 mm Mg^{2+} would require RyR1 open probability data at a large interval of Ca^{2+}, Mg^{2+}, and ATP concentrations, not presently available.

Implications

The structural analysis presented here explains the paradox of different sensitivity of RyR1 and RyR2 to inactivation by Ca^{2+} (Chu et al., 1993; Laver et al., 1997; Gomez and Yamaguchi, 2014; Gomez et al., 2016) when the Ca^{2+} binding affinity of the EF-hand region of both isoforms is identical (Xiong et al., 1998). Our data showed that the inactivation by divalent ions arises from the same substructures and proceeds by the same mechanism in both RyR isoforms, similar to the activation. In both activation and inactivation, the differences between isoforms emerge from the differences in the strength of the binding signal transmission to the channel gate. According to the COI model, in the case of activation, this influences the allosteric coefficient f_{Ca} that drives RyR opening, which is lower in RyR2 than in RyR1, and thus causes a higher maximum open probability of RyR2. In the case of inactivation, the difference is manifested in the lower allosteric coefficient h_M in RyR1 than in RyR2, which leads to a higher sensitivity to inactivation in RyR1 than in RyR2.

The limited data on RyR2 single-channel activity in the presence of ATP suggest that this ligand increases the transmission of the allosteric signal from the activation site, resulting in two effects: An increase of the apparent calcium sensitivity and maximum open probability, evoked by the decrease of the allosteric coefficient f_{Ca}, and an increase of the sensitivity to inactivation (decreased h_{CaM}) caused by the interaction between the Ca^{2+}-bound activation site and the M^{2+}-bound inhibition site. The increased sensitivity of RyR2 to Ca^{2+}-dependent inactivation in the presence of ATP is also supported by single-channel experiments (Chu et al., 1993; Gyorke and Gyorke, 1998). RyR channels can be considered mostly in the primed state under these conditions since the binding of ATP analogs induces the primed structural macrostate in RyRs even in the absence of Ca^{2+} (Cholak et al., 2023). Fortunately, the two sets of conditions for RyR2 open probability data that were available in the literature turned out to represent the activation of channels either selectively from the closed state (Fig. 10C), or selectively from the primed state (Fig. 10A, B). The primed state is structurally very close to the open state, and therefore the transitions between them should be energetically less demanding than the transitions between the structurally more different closed and open states. Precise determination of these effects would require

934 expanding the COI model to explicitly include the ATP binding site and the primed state; construction of
935 such a model is at present hampered by the lack of the RyR channel open probability data at a
936 sufficiently wide range of experimental conditions and the absence of high-resolution structures of WT
937 RyR2 in the primed state. Since the COI model does not contain explicit ATP-binding transitions, the
938 effect of ATP transpired only through the allosteric parameters f_{Ca} for Ca^{2+}-dependent activation and
939 h_{CaM} for M^{2+}-dependent inactivation.

940 The ATP site-containing branches of the activation pathway (A1 – A6, Table 5) appear responsible for the
941 synergy between the Ca^{2+} and ATP activating mechanisms in all RyR channels, as previously recognized
942 for the primed and open RyR1 structures (Chirasani et al., 2022). Our analysis reveals that this
943 interaction path also exists in the closed RyR structures 7k0t, 7vmm, and 7ua5 with the activation
944 binding site unoccupied by Ca^{2+}, in which the relative position of the C-terminal and Central domains
945 differs from the primed and open channels. This indicates that the molecular backbone for the
946 transmission of the activation allosteric signal is preexistent in all RyR gating states and that the Ca^{2+}
947 binding itself may constitute the signal that promotes the channel activation.

948 ## Limitations

949 The single-channel experiments, used here for deriving the model of RyR operation, were performed
950 under a limited number of experimental conditions that also slightly differed among laboratories. Only
951 experiments under two sets of conditions close to the physiological ones were included in the analysis
952 since RyR activity is sensitive to the ion composition and ionic strength of its environment (Ma et al.,
953 1993; Meissner et al., 1997; Liu et al., 1998). Experiments with purified RyR channels were neither
954 included for their different sensitivity to activation and inactivation by Ca^{2+} (Imagawa et al., 1987).

955 Due to the stochastic nature of the single-channel activity and the limited amount of available data, the
956 precision of some data used in this study might be influenced by natural variance, especially at low open
957 probability conditions. However, sufficiently exact measurements under conditions of low channel
958 activity would require the collection of a large amount of data (Zahradnikova et al., 2020) that might not
959 be experimentally feasible. Therefore, several parameters of the model of RyR operation had to be fixed
960 in this study at previously estimated values (Zahradnik et al., 2005; Iaparov et al., 2022). To determine
961 the relative importance of the intra- and inter-monomeric inhibition pathways would require
962 quantitative data on the effect of Mg^{2+} on RyR1 and RyR2 channels in the absence of ATP.

963 Unfortunately, it was not possible to use experimental data on ^{3}H-ryanodine binding for tuning the COI
964 model of RyR operation. First, the data from many laboratories do not present RyR inactivation, which
965 might be caused by the lengthy experimental procedure or by the presence of higher salt concentrations
966 (Murayama et al., 2018). Second, at least in some laboratories, activation of ^{3}H-ryanodine binding by
967 Mg^{2+} ions was observed (Chugun et al., 2007), an effect that has not been observed in the single-channel
968 measurements. Third, ^{3}H-ryanodine binding data are mostly presented relative to the maximum
969 observed binding, without providing the ^{3}H-ryanodine binding capacity B_{max} that would correspond to
970 the maximum of the channel open probability (P_o = 1).

971 At present, two problems of RyR inactivation have not been solved yet: Regarding the cardiac isoform,
972 no structure of the inhibited RyR2 was published till the present time. Despite observations of over 50%

973 inhibition by Ca^{2+} in the purified RyR2 channel at 10 mM Ca^{2+} in the absence of ATP (Xu et al., 1996), or
974 even at 1 mM Ca^{2+} in the native RyR2 channel in the presence of ATP (Gyorke and Gyorke, 1998), the
975 only RyR2 structure published at 5 mM Ca^{2+} in the presence of ATP and caffeine represented the open
976 and not the inactivated state (Gong et al., 2019). Regarding the skeletal muscle isoform, no electron
977 densities attributable to ions bound at the EF-hand loops were observed either in the Ca^{2+}-inactivated
978 RyR1 (Nayak and Samso, 2022) or the Mg^{2+}-inactivated RyR1 (Nayak et al., 2024). However, the local
979 resolution of the electron density map is insufficient to decide unequivocally whether Ca^{2+} ions are
980 present or not in the structure of the apparent ion binding inhibition site.

981 ## Concluding remarks

982 The existence of the comprehensive model of mammalian RyR operation puts together the partial
983 observations on RyR structures, equilibrium binding studies, and single-channel gating activity, collected
984 across species and over the years by many independent laboratories.

985 The methods of bioinformatic analysis applied to numerous RyR structures have shown that in both RyR
986 isoforms, the inhibitory binding site for divalent ions is very likely formed by the EF1 and EF2 loops. The
987 transmission of the inhibition signal to the channel gate proceeds through two pathways: the inter-
988 monomeric pathway that leads through the interface between the EF-hand region and the S23* loop,
989 and the intra-monomeric pathway that converges with the Ca^{2+}-activation pathway. The difference
990 between RyR1 and RyR2 inhibition by divalent ions is caused by the different coupling efficiency of the
991 inhibition pathways in RyR1 and RyR2.

992 RyR1 and RyR2 structures present a peculiar construction of their core that controls the RyR channel
993 activity in dependence on the cytosolic concentration of Ca^{2+} and Mg^{2+} ions and endogenous modulators
994 like ATP and xanthines. Each RyR monomer has specific binding sites for these ligands connected to the
995 channel gate by a common allosteric network. Changes in the ligand occupation of binding sites drive
996 stochastic transitions of RyR monomers among the closed – primed – open – inactivated macrostates
997 towards the energetically more preferable state. This means that RyR can assume any macrostate with
998 some probability for a time under any experimental conditions. The macrostate of monomers in the RyR
999 homo-tetramer does change in synchrony, by a structural process supported by the inter-monomeric
1000 coupling of allosteric networks. Recent data point to the central role of the U-motif at which the intra-
1001 monomeric and inter-monomeric allosteric networks merge and thus allow for the exchange of energy.

1002 # Materials and Methods

1003 ## Bioinformatics analyses

1004 Ryanodine receptor sequences were taken from the UniProt database (https://www.uniprot.org/) and
1005 aligned using CLUSTAL Omega at EMBL-EBI (https://www.ebi.ac.uk/jdispatcher/msa/clustalo; (Sievers et
1006 al., 2011)) relative to rabbit RyR1. The residue numbers of the examined domains are given in Table 8 for
1007 the studied species/isoforms.

Table 8. Sequence numbers of the ryanodine receptor core domains.

Domain	rRyR1	mRyR2	hRyR2	pRyR2, rRyR2
Central domain (CD)	3668-4070	3634-4024	3635-4025	3636-4026
EF-hand region (EF)	4071-4131	4025-4085	4026-4086	4027-4087
U-motif (U)	4132-4251	4086-4205	4087-4206	4088-4207
S23 loop (S23)	4663-4786	4591-4715	4592-4716	4593-4717
S45 linker (S45)	4821-4834	4750-4763	4751-4764	4752-4765
S6 segment (S6)	4910-4956	4839-4885	4840-4886	4841-4887
C-terminal domain (CTD)	4957-5033	4886-4962	4887-4963	4888-4964

Prefixes r, m, h, and p refer to rabbit, mouse, human, and pig.

1008 Sequence identities of RyR isoforms were calculated using the SIAS server
1009 (http://imed.med.ucm.es/Tools/sias.html). In the text, sequence numbers are given for the rabbit RyR1
1010 (rRyR1) and human RyR2 (hRyR2), if not indicated otherwise.

1011 Structures of ryanodine receptors were obtained from the protein data bank (https://www.rcsb.org/).
1012 To ensure compatibility of structural and functional data, we have considered and used those RyR
1013 structures that were either ligand-free or contained Ca^{2+}-, Mg^{2+}, caffeine (xanthine), ATP (ACP) visible in
1014 their structure or were obtained in the presence of these ligands or their combination (Expanded View
1015 Dataset EV1). These included 26 structures of rabbit RyR1 (des Georges et al., 2016; Melville et al.,
1016 2022a; Melville et al., 2022b; Nayak and Samso, 2022), 7 structures of pig RyR2 (Peng et al., 2016; Gong
1017 et al., 2019), 5 structures of human RyR2 (Miotto et al., 2022) and 5 structures of mouse RyR2
1018 (Kobayashi et al., 2022). The resolution of these structures was reported in the range of 2.45 - 6.2 Å.
1019 Structures of mutant RyRs, or structures obtained in the presence of ryanodine, ruthenium red, or the
1020 activator pentachlorobiphenyl, and structures with unresolved critical amino acid side chains were not
1021 included.

1022 The flexion angle between the horizontal plane and the line formed by Cα atoms of residues
1023 corresponding to rRyR1 residues 348 and 1052 (Steele and Samso, 2019) was measured manually in
1024 Chimera Ver. 1.17 (Pettersen et al., 2004) (https://www.rbvi.ucsf.edu/chimera) and is shown in
1025 Expanded View Dataset EV1.

1026 Editing and optimization of structures were performed in Chimera as follows: The monomer core (the C-
1027 terminal quarter residues 3639 – 5037; (Du and Maclennan, 1999)) or its selected part was cut out from
1028 the whole RyR structure. In model structures used for the determination of allosteric pathways, the

1029 short unresolved loops were reconstructed to correspond to the known sequence, and the missing long
1030 part of the unresolved DR1 region was replaced by a polyglycine loop. The reconstructed loops were
1031 optimized using the program MODELLER (Sali and Blundell, 1993) or the server MODLOOP
1032 (https://modbase.compbio.ucsf.edu/modloop/ (Fiser et al., 2000; Fiser and Sali, 2003)). The edited
1033 structures were repaired by adding missing atoms to incomplete residues. Finally, hydrogens and
1034 appropriate charges were added. Selective residue mutations were introduced to the studied segments
1035 of interest in Chimera.

1036 The repaired model structures were energy-minimized using at least 1000 iterations of steepest descent
1037 and 100 iterations of maximum gradient minimization with fixed positions of the first five and last five
1038 Cα atoms. The resulting model structures were used for different types of analysis as indicated in
1039 Expanded View Dataset EV1.

1040 The maximum distance between Cα atoms of H-bond-forming electron donor residues glutamate or
1041 aspartate and the electron acceptor residues lysine or arginine was calculated as follows: The distance
1042 from the Cα atom to the farthest oxygen atom of the electron donor residue (d_D), and the distance from
1043 the Cα atom to the farthest nitrogen atom of the electron acceptor residue (d_A) in their extended
1044 configurations were measured. The maximum distance was calculated as the sum ($d_D + d_A + 2.7$) Å,
1045 where 2.7 Å is the standard length of a hydrogen bond.

1046 The EF-hand identity score (IS) was calculated according to the scoring system of Zhou et al. (2006),
1047 which compares the identity of amino acids in the ion-binding loop of the examined EF-hand sequence
1048 with the 12 amino acids of the canonical EF-hand loop (EF-hand PROSITE pattern PS00018) or their
1049 allowed equivalents (D, N, S at position 1, and any residue at position 2). The resulting identity score
1050 consists of three numbers x/y/z. The value of x (0 - 12) reports the number of amino acids concurring at
1051 their given positions with amino acids of the allowed EF-hand loop residues. The value of y (0 - 6)
1052 reports the number of amino acids concurring with the 6 amino acids of the loop in positions 1, 3, 5, 7,
1053 9, and 12, involved in divalent ion binding. The value of z (0 - 3) compares the amino acid concurrence at
1054 positions 1, 3, and 12, considered critical for ion binding. Thus, a canonical EF-hand, such as that of
1055 calmodulin, provides the highest EF-hand identity score of 12/6/3. We report the IS together with the
1056 sum of the partial scores in the form of x/y/z (x+y+z).

1057 The ion binding score (IBS) and the number of ion binding poses (NIBP) of EF-hand loops were estimated
1058 on edited and energy-optimized model structures using the MIB2 server
1059 http://combio.life.nctu.edu.tw/MIB2/ (Lu et al., 2022) as follows: first, the EF-hand region and 31
1060 subsequent residues ending with a β-hairpin, corresponding to rabbit RyR1 residues 4032-4182, were
1061 isolated from the selected RyR structures (Expanded View Dataset EV1). This segment was chosen for its
1062 expected structural stability. The optimized EF-hand structure was uploaded to the MIB2 server, which
1063 returned the ion-binding scores for all individual residues and the number of acceptable ion-binding
1064 poses.

1065 Electrostatic interactions as well as the interface area between the interacting EF-hand region and S23
1066 loop were quantified on edited and optimized structures using the server PDBePISA
1067 (https://www.ebi.ac.uk/msd-srv/prot_int/cgi-bin/piserver). The examined structures contained residues
1068 4032-4182 of the extended EF-hand region and residues 4695-4745 of the S23* loop.

1069 Root-mean-square deviations (RMSD) were estimated on unedited original structures in Chimera (Ver. 1.
1070 17). The examined structures were aligned through the Cα atoms of their Central domain residues
1071 (corresponding to rRyR1 residues 3668-3679, 3694-3733, 3753-3855, and 3873-4070, which were
1072 resolved in all RyR structures) with the corresponding Cα atoms of the reference RyR structures 7k0t
1073 (closed RyR1) and 7tdg (inactivated RyR1). The RMSD between Cα atoms of the examined RyR domains
1074 in different structural states and the corresponding Cα atoms of the reference RyR structures were
1075 calculated. RMSD calculation of the S23 loop was performed only on residues 4716-4754, positioned in
1076 the vicinity of the neighbor monomer, since the rest of the S23 loop was not well-resolved in all
1077 structures. Otherwise, the domain residues were specified according to Table 8. The RMSD values were
1078 normalized for 100 amino acid residues (Carugo and Pongor, 2001) to account for differences in the
1079 length of individual domains, and denoted as 7k0t-$RMSD_{100}$ or 7tdg-$RMSD_{100}$ for alignment with 7k0t or
1080 7tdg, respectively. Only $RMSD_{100}$ values larger than 2 Å were considered to indicate a significant
1081 structural change (Carugo, 2007).

1082 Allosteric pathways were traced using the server OHM (https://dokhlab.med.psu.edu/ohm/#/home,
1083 (Wang et al., 2020)), in which the allosteric pathway is determined on the basis of the network of
1084 contacts between pairs of residues in the given structure. Five RyR1 and four RyR2 structures with the
1085 best resolution and the lowest number of unresolved residues were selected from the studied set
1086 (Expanded View Dataset EV1) and processed for analysis. Two copies of the monomer core were aligned
1087 to two adjacent monomers of the original RyR tetrameric structure. The resulting dimers were subjected
1088 to energy minimization in Chimera Ver. 1.17 until all clashes were removed. Finally, the optimized model
1089 structures were uploaded to the OHM server to trace the sequences of residues connecting the
1090 allosteric site of interest with the active site. As the allosteric site, either the residues of the EF1 and EF2
1091 loops (INH) as the putative divalent ion binding inhibition site or the CD and CTD residues of the Ca^{2+}-
1092 binding activation site (ACT) (Wang et al., 2020; Chirasani et al., 2022) were selected. As the active site,
1093 the gate and hinge residues of the S6 segment (Table 9) were selected. The simulation of the
1094 perturbation propagation for calculating the residue importance was performed 10 000 times per
1095 structure.

1096 The output of the OHM server consisted of two items for each RyR structure: (1) The list of the first 100
1097 most important allosteric pathways ("paths.txt"), in which a chain of interacting residues represented
1098 the individual pathway. This list was used for sorting paths by important residues and estimating the
1099 fraction of major pathways and branches. (2) The description of the complete allosteric network
1100 ("net.txt"), consisting of the list of critical residues of the allosteric network with their respective residue
1101 importance (RI), and the list of network edges, showing connections between the residues in the
1102 pathway. The network list was used to select the residues with the highest RI and examine their
1103 connections within the pathways. In addition to these outputs, the graph of the allosteric network for a
1104 selected set of pathways (3, 5, 7, 10, 20, 30, 40, 50, 60, 70, 80, 90, or all of the 100 listed pathways) was
1105 visually examined to understand the meaning of different pathways in the context of all possible
1106 pathways. The fractional contribution of critical residues (output list "_net.txt") functionally and
1107 structurally important to the allosteric network was calculated as the frequency of their occurrence in
1108 the first 100 most frequently occurring pathways (output list "_paths.txt"). The output files "_net.txt"
1109 and "_paths.txt" are located in the file Expanded View Dataset EV2.

Table 9. The residues of the allosteric and active sites (rRyR1 numbering)

Allosteric sites	**Residues**
INH: EF-hand loops	4081-4092, 4116-4127
ACT: Ca^{2+} activation site	**3893, 3967**, 3970, **5001**, 5002
Active site	
GATE: S6 Hinge and Gate	G4934, G4934*, I4937, I4937*

Residues with * belong to the monomer neighboring the monomer bearing the analyzed allosteric site.
Residue numbers in bold were originally defined as the Ca^{2+} binding site-forming residues by (des Georges et al., 2016).

1110 ## Modeling the RyR operation

1111 The model of RyR operation was constructed on the Monod-Wyman-Changeaux (MWC) theorem
1112 (Monod et al., 1965) and homo-tetrameric Markovian memory-free mechanism (Zahradnik et al., 2005;
1113 Zahradnikova et al., 2010) using a statistical mechanics approach (Marzen et al., 2013; Iaparov et al.,
1114 2022). The model presumes an allosteric mechanism where ions activating and/or inhibiting RyR
1115 opening bind to the specific regulatory sites present on each monomer and exert their effect by
1116 allosteric coupling to the remote gating site. The gating site of the RyR pore should be in the open
1117 position in all four monomers to make the ion permeation possible. The free energy of ion binding to
1118 the specific binding site is supposed to be independent of the identity of the monomer and the
1119 presence/absence of ligands at the binding sites of other monomers but is supposed to depend on the
1120 macrostate of the whole RyR. Mathematically, all possible macrostates pre-exist in the absence of
1121 ligands and the binding of a ligand affects the relative occurrence of a given macrostate by altering its
1122 free energy. A transition between macrostates occurs in a concerted manner at all monomers (Hilser et
1123 al., 2012). This supposition greatly reduces the number of considered macrostates and reduces demands
1124 on computational power.

1125 The dependence of the RyR open probability on the concentration of regulatory ions was described
1126 using the framework of statistical mechanics (Marzen et al., 2013; Iaparov et al., 2022). The parameters
1127 of the model equations (see Results) were optimized using the Levenberg-Marquardt method for the
1128 best fit of the RyR single-channel open probability data in OriginPro (ver. 2022b). The simple shape of
1129 the calcium dependence of open probability and the limited size of available experimental data led to
1130 the mutual dependence of some fitted parameters and non-convergence of the fit. To solve this
1131 problem, the number of free parameters was reduced as described in the Results. A global fit of the
1132 whole dataset was then performed with the minimal chi-square value as the minimization criterion for
1133 the whole dataset.

1134 ## Statistical analysis

1135 One-way ANOVA was performed in Origin (OriginLab, V. 2024) to test the significance of the differences
1136 between groups. The test was performed only if the distribution of data did not significantly deviate
1137 from normality (Shapiro-Wilk test), and if the population variances were not significantly different
1138 (Levene's test). Comparison of means was performed with Scheffe's test. Values with $p < 0.05$ were

1139 considered significant. The power of the test was calculated at $\alpha = 0.05$ and had to be > 0.95 to accept
1140 the ANOVA results. If the distribution of data deviated from normality, the Kruskal-Wallis ANOVA
1141 followed by Dunn's test were used instead.

Acknowledgments

The authors would like to thank Dr. N. V. Dokholyan and Dr. V.R. Chirasani for their help with using the OHM server, and to Dr. B. Iaparov for the help with using statistical mechanics.

This work was supported by the Turkish-Slovak Joint Partnership of The Scientific and Technological Research Council of Turkey (TÜBİTAK) and Slovak Academy of Sciences grant JRP/2019/836/RyRinHeart and TÜBİTAK grant number 119Z578, and by the projects APVV-21-0443 from the Slovak Research and Development Agency, and VEGA 2/20182/21 from the Ministry of Education, Research, Development and Youth of the Slovak Republic and Slovak Academy of Sciences.

Author contributions

A.Z. and I.Z. conceived and designed the study; A.Z. supervised the study, created the structural models, performed structural analysis and visualization, and designed, derived, and validated the statistical mechanics model; A.Z. and J.P. performed server-based bioinformatics analysis; A.Z., J.P. and M.S. validated the bioinformatics analysis; S.B. performed molecular simulations and provided valuable intellectual input; A.Z. and I.Z. interpreted the data and wrote the manuscript; S.B. reviewed and edited the manuscript.

Competing interests

The authors declare no competing interests.

Author ORCIDs

Alexandra Zahradníková: https://orcid.org/0000-0002-7296-9617
Jana Pavelková: https://orcid.org/0000-0002-9539-2312
Miroslav Sabo: https://orcid.org/0009-0009-2112-2502
Sefer Baday: https://orcid.org/0000-0002-2913-6687
Ivan Zahradník: https://orcid.org/0000-0001-5125-9467

Supplementary Information

Supplementary Information contains Expanded View Figures EV1 and EV2 that complement Figure 8 and Figure 9, respectively; Expanded View Dataset EV1 that lists the structures used in this study and their characteristics and Expanded View Dataset EV2 that contains the output of the OHM server used in the analysis of allosteric pathways, Appendix PDF that contains Appendix Tables S1 – S3 that complement Tables 4 – 6, respectively, and Expanded View Movies EV1 and EV2 that complement Figure 8.

Data availability

The data that support this study are available from the corresponding authors upon request. Previously published protein structure data used for analysis in this study are available in the Protein Data Bank under accession codes listed in Expanded View Dataset EV1.

1175 ## References

1176 Bai, X.C., Z. Yan, J. Wu, Z. Li, and N. Yan. 2016. The Central domain of RyR1 is the transducer for long-
1177 range allosteric gating of channel opening. *Cell Res*. 26:995-1006. doi: 10.1038/cr.2016.89.

1178 Bers, D.M., C.W. Patton, and R. Nuccitelli. 1994. A practical guide to the preparation of Ca2+ buffers.
1179 *Methods Cell Biol*. 40:3-29. doi: 10.1016/s0091-679x(08)61108-5.

1180 Carugo, O. 2007. Statistical validation of the root-mean-square-distance, a measure of protein structural
1181 proximity. *Protein Eng Des Sel*. 20:33-37. doi: 10.1093/protein/gzl051.

1182 Carugo, O., and S. Pongor. 2001. A normalized root-mean-square distance for comparing protein three-
1183 dimensional structures. *Protein Sci*. 10:1470-1473. doi: 10.1110/ps.690101.

1184 Chi, X., D. Gong, K. Ren, G. Zhou, G. Huang, J. Lei, Q. Zhou, and N. Yan. 2019. Molecular basis for
1185 allosteric regulation of the type 2 ryanodine receptor channel gating by key modulators. *Proc*
1186 *Natl Acad Sci U S A*. 116:25575-25582. doi: 10.1073/pnas.1914451116.

1187 Chirasani, V.R., M. Elferdink, M. Kral, J.S. Carter, S. Heitmann, G. Meissner, and N. Yamaguchi. 2024
1188 Structural and functional interactions between the EF hand domain and S2-S3 loop in the type-1
1189 ryanodine receptor ion channel. *J Biol Chem*. 300:105606. doi: 10.1016/j.jbc.2023.105606.

1190 Chirasani, V.R., K.I. Popov, G. Meissner, and N.V. Dokholyan. 2022. Mapping co-regulatory interactions
1191 among ligand-binding sites in ryanodine receptor 1. *Proteins*. 90:385-394. doi:
1192 10.1002/prot.26228.

1193 Cholak, S., J.W. Saville, X. Zhu, A.M. Berezuk, K.S. Tuttle, O. Haji-Ghassemi, F.J. Alvarado, F. Van Petegem,
1194 and S. Subramaniam. 2023. Allosteric modulation of ryanodine receptor RyR1 by nucleotide
1195 derivatives. *Structure*. 31:790-800 e794. doi: 10.1016/j.str.2023.04.009.

1196 Chu, A., M. Fill, E. Stefani, and M.L. Entman. 1993. Cytoplasmic Ca2+ does not inhibit the cardiac muscle
1197 sarcoplasmic reticulum ryanodine receptor Ca2+ channel, although Ca2+-induced Ca2+
1198 inactivation of Ca2+ release is observed in native vesicles. *Journal of Membrane Biology*. 135:49-
1199 59. doi:

1200 Chugun, A., O. Sato, H. Takeshima, and Y. Ogawa. 2007. Mg2+ activates the ryanodine receptor type 2
1201 (RyR2) at intermediate Ca2+ concentrations. *Am J Physiol Cell Physiol*. 292:C535-544. doi:

1202 Dashti, A., G. Mashayekhi, M. Shekhar, D. Ben Hail, S. Salah, P. Schwander, A. des Georges, A. Singharoy,
1203 J. Frank, and A. Ourmazd. 2020. Retrieving functional pathways of biomolecules from single-
1204 particle snapshots. *Nat Commun*. 11:4734. doi: 10.1038/s41467-020-18403-x.

1205 des Georges, A., O.B. Clarke, R. Zalk, Q. Yuan, K.J. Condon, R.A. Grassucci, W.A. Hendrickson, A.R. Marks,
1206 and J. Frank. 2016. Structural Basis for Gating and Activation of RyR1. *Cell*. 167:145-157 e117.
1207 doi: 10.1016/j.cell.2016.08.075.

1208 Du, G.G., and D.H. Maclennan. 1999. Ca(2+) inactivation sites are located in the COOH-terminal quarter
1209 of recombinant rabbit skeletal muscle Ca(2+) release channels (ryanodine receptors). *Journal of*
1210 *Biological Chemistry*. 274:26120-26126. doi:

1211 Efremov, R.G., A. Leitner, R. Aebersold, and S. Raunser. 2015. Architecture and conformational switch
1212 mechanism of the ryanodine receptor. *Nature*. 517:39-43. doi: 10.1038/nature13916.

1213 Fessenden, J.D., W. Feng, I.N. Pessah, and P.D. Allen. 2004. Mutational analysis of putative calcium
1214 binding motifs within the skeletal ryanodine receptor isoform, RyR1. *J Biol Chem*. 279:53028-
1215 53035. doi: 10.1074/jbc.M411136200.

1216 Fill, M., E. Stefani, and T.E. Nelson. 1991. Abnormal human sarcoplasmic reticulum Ca2+ release
1217 channels in malignant hyperthermic skeletal muscle. *Biophysical Journal*. 59:1085-1090. doi:

1218 Fiser, A., R.K. Do, and A. Sali. 2000. Modeling of loops in protein structures. *Protein Sci*. 9:1753-1773.
1219 doi: 10.1110/ps.9.9.1753.

1220 Fiser, A., and A. Sali. 2003. ModLoop: automated modeling of loops in protein structures. *Bioinformatics*.
1221 19:2500-2501. doi: 10.1093/bioinformatics/btg362.

1222 George, C.H., H. Jundi, N.L. Thomas, D.L. Fry, and F.A. Lai. 2007. Ryanodine receptors and ventricular
1223 arrhythmias: Emerging trends in mutations, mechanisms and therapies. *Journal of Molecular*
1224 *and Cellular Cardiology*. .42:34-50. doi:

1225 Gillespie, D. 2020. Recruiting RyRs to Open in a Ca(2+) Release Unit: Single-RyR Gating Properties Make
1226 RyR Group Dynamics. *Biophys J*. 118:232-242. doi: 10.1016/j.bpj.2019.11.021.

1227 Gillespie, D., and M. Fill. 2013. Pernicious attrition and inter-RyR2 CICR current control in cardiac muscle.
1228 *J Mol Cell Cardiol*. 58:53-58. doi: 10.1016/j.yjmcc.2013.01.011.

1229 Gomez, A.C., T.W. Holford, and N. Yamaguchi. 2016. Malignant hyperthermia-associated mutations in
1230 the S2-S3 cytoplasmic loop of type 1 ryanodine receptor calcium channel impair calcium-
1231 dependent inactivation. *Am J Physiol Cell Physiol*. 311:C749-C757. doi:
1232 10.1152/ajpcell.00134.2016.

1233 Gomez, A.C., and N. Yamaguchi. 2014. Two regions of the ryanodine receptor calcium channel are
1234 involved in Ca(2+)-dependent inactivation. *Biochemistry*. 53:1373-1379. doi:
1235 10.1021/bi401586h.

1236 Gong, D., X. Chi, J. Wei, G. Zhou, G. Huang, L. Zhang, R. Wang, J. Lei, S.R.W. Chen, and N. Yan. 2019.
1237 Modulation of cardiac ryanodine receptor 2 by calmodulin. *Nature*. 572:347-351. doi:
1238 10.1038/s41586-019-1377-y.

1239 Greene, D., M. Barton, T. Luchko, and Y. Shiferaw. 2022. Molecular Dynamics Simulations of the Cardiac
1240 Ryanodine Receptor Type 2 (RyR2) Gating Mechanism. *J Phys Chem B*. 126:9790-9809. doi:
1241 10.1021/acs.jpcb.2c03031.

1242 Guo, W., B. Sun, J.P. Estillore, R. Wang, and S.R.W. Chen. 2020. The central domain of cardiac ryanodine
1243 receptor governs channel activation, regulation, and stability. *J Biol Chem*. 295:15622-15635.
1244 doi: 10.1074/jbc.RA120.013512.

1245 Gyorke, I., and S. Gyorke. 1998. Regulation of the cardiac ryanodine receptor channel by luminal Ca2+
1246 involves luminal Ca2+ sensing sites. *Biophysical Journal*. 75:2801-2810. doi:

1247 Hadiatullah, H., Z. He, and Z. Yuchi. 2022. Structural Insight Into Ryanodine Receptor Channelopathies.
1248 *Front Pharmacol*. 13:897494. doi: 10.3389/fphar.2022.897494.

1249 Haji-Ghassemi, O., Y.S. Chen, K. Woll, G.B. Gurrola, C.R. Valdivia, W. Cai, S. Li, H.H. Valdivia, and F. Van
1250 Petegem. 2023. Cryo-EM analysis of scorpion toxin binding to Ryanodine Receptors reveals
1251 subconductance that is abolished by PKA phosphorylation. *Sci Adv*. 9:eadf4936. doi:
1252 10.1126/sciadv.adf4936.

1253 Hilser, V.J., J.O. Wrabl, and H.N. Motlagh. 2012. Structural and energetic basis of allostery. *Annu Rev*
1254 *Biophys*. 41:585-609. doi: 10.1146/annurev-biophys-050511-102319.

1255 Horrigan, F.T., and R.W. Aldrich. 2002. Coupling between voltage sensor activation, Ca2+ binding and
1256 channel opening in large conductance (BK) potassium channels. *J Gen Physiol*. 120:267-305. doi:
1257 10.1085/jgp.20028605.

1258 Iaparov, B., I. Baglaeva, I. Zahradnik, and A. Zahradnikova. 2022. Magnesium Ions Moderate Calcium-
1259 Induced Calcium Release in Cardiac Calcium Release Sites by Binding to Ryanodine Receptor
1260 Activation and Inhibition Sites. *Front Physiol*. 12:805956. doi: 10.3389/fphys.2021.805956.

1261 Ikemoto, N., and T. Yamamoto. 2000. Postulated role of inter-domain interaction within the ryanodine
1262 receptor in Ca(2+) channel regulation. *Trends Cardiovasc Med*. 10:310-316. doi:

1263 Imagawa, T., J.S. Smith, R. Coronado, and K.P. Campbell. 1987. Purified ryanodine receptor from skeletal
1264 muscle sarcoplasmic reticulum is the Ca2+ -permeable pore of the calcium release channel.
1265 *Journal of Biological Chemistry*. 262:16636-16643. doi:

1266 Iyer, K.A., V. Barnakov, and M. Samso. 2023. Three-dimensional perspective on ryanodine receptor
1267 mutations causing skeletal and cardiac muscle-related diseases. *Curr Opin Pharmacol*.
1268 68:102327. doi: 10.1016/j.coph.2022.102327.

1269 Iyer, K.A., Y. Hu, A.R. Nayak, N. Kurebayashi, T. Murayama, and M. Samso. 2020. Structural mechanism
1270 of two gain-of-function cardiac and skeletal RyR mutations at an equivalent site by cryo-EM. *Sci*
1271 *Adv*. 6:eabb2964. doi: 10.1126/sciadv.abb2964.

1272 Kobayashi, T., A. Tsutsumi, N. Kurebayashi, K. Saito, M. Kodama, T. Sakurai, M. Kikkawa, T. Murayama,
1273 and H. Ogawa. 2022. Molecular basis for gating of cardiac ryanodine receptor explains the
1274 mechanisms for gain- and loss-of function mutations. *Nat Commun*. 13:2821. doi:
1275 10.1038/s41467-022-30429-x.

1276 Kubalova, Z., D. Terentyev, S. Viatchenko-Karpinski, Y. Nishijima, I. Gyorke, R. Terentyeva, D.N. da Cunha,
1277 A. Sridhar, D.S. Feldman, R.L. Hamlin, C.A. Carnes, and S. Gyorke. 2005. Abnormal intrastore
1278 calcium signaling in chronic heart failure. *Proc.Natl.Acad.Sci U.S.A*. 102:14104-14109. doi:

1279 Laver, D.R., T.M. Baynes, and A.F. Dulhunty. 1997. Magnesium inhibition of ryanodine-receptor calcium
1280 channels: Evidence for two independent mechanisms. *J.Membrane.Biol*. 156:213-229. doi:

1281 Laver, D.R., C.H. Kong, M.S. Imtiaz, and M.B. Cannell. 2013. Termination of calcium-induced calcium
1282 release by induction decay: an emergent property of stochastic channel gating and molecular
1283 scale architecture. *J Mol Cell Cardiol*. 54:98-100. doi: 10.1016/j.yjmcc.2012.10.009.

1284 Laver, D.R., L.D. Roden, G.P. Ahern, K.R. Eager, P.R. Junankar, and A.F. Dulhunty. 1995. Cytoplasmic Ca2+
1285 inhibits the ryanodine receptor from cardiac muscle. *J.Membrane.Biol*. 147:7-22. doi:

1286 Lehnart, S.E., X.H. Wehrens, P.J. Laitinen, S.R. Reiken, S.X. Deng, Z. Cheng, D.W. Landry, K. Kontula, H.
1287 Swan, and A.R. Marks. 2004. Sudden death in familial polymorphic ventricular tachycardia
1288 associated with calcium release channel (ryanodine receptor) leak. *Circulation*. 109:3208-3214.
1289 doi:

1290 Li, J., M.S. Imtiaz, N.A. Beard, A.F. Dulhunty, R. Thorne, D.F. vanHelden, and D.R. Laver. 2013. ss-
1291 Adrenergic stimulation increases RyR2 activity via intracellular Ca2+ and Mg2+ regulation. *PLoS*
1292 *One*. 8:e58334. doi: 10.1371/journal.pone.0058334.

1293 Lin, Y.F., C.W. Cheng, C.S. Shih, J.K. Hwang, C.S. Yu, and C.H. Lu. 2016. MIB: Metal Ion-Binding Site
1294 Prediction and Docking Server. *J Chem Inf Model*. 56:2287-2291. doi: 10.1021/acs.jcim.6b00407.

1295 Liu, W., D.A. Pasek, and G. Meissner. 1998. Modulation of Ca(2+)-gated cardiac muscle Ca(2+)-release
1296 channel (ryanodine receptor) by mono- and divalent ions. *American Journal of Physiology*.
1297 274:C120-C128. doi:

1298 Lu, C.H., C.C. Chen, C.S. Yu, Y.Y. Liu, J.J. Liu, S.T. Wei, and Y.F. Lin. 2022. MIB2: metal ion-binding site
1299 prediction and modeling server. *Bioinformatics*. 38:4428-4429. doi:
1300 10.1093/bioinformatics/btac534.

1301 Lu, C.H., Y.F. Lin, J.J. Lin, and C.S. Yu. 2012. Prediction of metal ion-binding sites in proteins using the
1302 fragment transformation method. *PLoS One*. 7:e39252. doi: 10.1371/journal.pone.0039252.

1303 Ma, J., K. Anderson, R. Shirokov, R. Levis, A. Gonzalez, M. Karhanek, M.M. Hosey, G. Meissner, and E.
1304 Rios. 1993. Effects of perchlorate on the molecules of excitation-contraction coupling of skeletal
1305 and cardiac muscle. *Journal of General Physiology*. 102:423-448. doi:

1306 Ma, R., O. Haji-Ghassemi, D. Ma, H. Jiang, L. Lin, L. Yao, A. Samurkas, Y. Li, Y. Wang, P. Cao, S. Wu, Y.
1307 Zhang, T. Murayama, B. Moussian, F. Van Petegem, and Z. Yuchi. 2020. Structural basis for
1308 diamide modulation of ryanodine receptor. *Nat Chem Biol*. 16:1246-1254. doi: 10.1038/s41589-
1309 020-0627-5.

1310 Marzen, S., H.G. Garcia, and R. Phillips. 2013. Statistical mechanics of Monod-Wyman-Changeux (MWC)
1311 models. *J Mol Biol*. 425:1433-1460. doi: 10.1016/j.jmb.2013.03.013.

1312 Meissner, G. 2017. The structural basis of ryanodine receptor ion channel function. *J Gen Physiol*.
1313 149:1065-1089. doi: 10.1085/jgp.201711878.

1314 Meissner, G., E. Rios, A. Tripathy, and D.A. Pasek. 1997. Regulation of skeletal muscle Ca2+ release
1315 channel (ryanodine receptor) by Ca2+ and monovalent cations and anions. *J.Biol Chem.*
1316 272:1628-1638. doi:

1317 Melville, Z., H. Dridi, Q. Yuan, S. Reiken, A. Wronska, Y. Liu, O.B. Clarke, and A.R. Marks. 2022a. A drug
1318 and ATP binding site in type 1 ryanodine receptor. *Structure*. 30:1025-1034 e1024. doi:
1319 10.1016/j.str.2022.04.010.

1320 Melville, Z., K. Kim, O.B. Clarke, and A.R. Marks. 2022b. High-resolution structure of the membrane-
1321 embedded skeletal muscle ryanodine receptor. *Structure*. 30:172-180 e173. doi:
1322 10.1016/j.str.2021.08.001.

1323 Miotto, M.C., G. Weninger, H. Dridi, Q. Yuan, Y. Liu, A. Wronska, Z. Melville, L. Sittenfeld, S. Reiken, and
1324 A.R. Marks. 2022. Structural analyses of human ryanodine receptor type 2 channels reveal the
1325 mechanisms for sudden cardiac death and treatment. *Sci Adv*. 8:eabo1272. doi:
1326 10.1126/sciadv.abo1272.

1327 Monod, J., J. Wyman, and J.P. Changeux. 1965. On the Nature of Allosteric Transitions: A Plausible
1328 Model. *J Mol Biol*. 12:88-118. doi: 10.1016/s0022-2836(65)80285-6.

1329 Murayama, T., N. Kurebayashi, T. Oba, H. Oyamada, K. Oguchi, T. Sakurai, and Y. Ogawa. 2011. Role of
1330 amino-terminal half of the S4-S5 linker in type 1 ryanodine receptor (RyR1) channel gating. *J Biol*
1331 *Chem*. 286:35571-35577. doi: 10.1074/jbc.M111.255240.

1332 Murayama, T., H. Ogawa, N. Kurebayashi, S. Ohno, M. Horie, and T. Sakurai. 2018. A tryptophan residue
1333 in the caffeine-binding site of the ryanodine receptor regulates Ca(2+) sensitivity. *Commun Biol*.
1334 1:98. doi: 10.1038/s42003-018-0103-x.

1335 Nayak, A.R., W. Rangubpit, A.H. Will, Y. Hu, P. Castro-Hartmann, J.J. Lobo, K. Dryden, G.D. Lamb, P.
1336 Sompornpisut, and M. Samso. 2024. Interplay between Mg(2+) and Ca(2+) at multiple sites of
1337 the ryanodine receptor. *Nat Commun*. 15:4115. doi: 10.1038/s41467-024-48292-3.

1338 Nayak, A.R., and M. Samso. 2022. Ca(2+) inactivation of the mammalian ryanodine receptor type 1 in a
1339 lipidic environment revealed by cryo-EM. *Elife*. 11. doi: 10.7554/eLife.75568.

1340 Niggli, E., N.D. Ullrich, D. Gutierrez, S. Kyrychenko, E. Polakova, and N. Shirokova. 2013. Posttranslational
1341 modifications of cardiac ryanodine receptors: Ca(2+) signaling and EC-coupling. *Biochim Biophys*
1342 *Acta*. 1833:866-875. doi: 10.1016/j.bbamcr.2012.08.016.

1343 Peng, W., H. Shen, J. Wu, W. Guo, X. Pan, R. Wang, S.R. Chen, and N. Yan. 2016. Structural basis for the
1344 gating mechanism of the type 2 ryanodine receptor RyR2. *Science*. 354. doi:
1345 10.1126/science.aah5324.

1346 Pettersen, E.F., T.D. Goddard, C.C. Huang, G.S. Couch, D.M. Greenblatt, E.C. Meng, and T.E. Ferrin. 2004.
1347 UCSF Chimera--a visualization system for exploratory research and analysis. *J Comput Chem*.
1348 25:1605-1612. doi: 10.1002/jcc.20084.

1349 Rios, E., and M.D. Stern. 1997. Calcium in close quarters: microdomain feedback in excitation-
1350 contraction coupling and other cell biological phenomena. *Annu.Rev.Biophys.Biomol.Struct.*
1351 26:47-82. doi:

1352 Robinson, R., D. Carpenter, M.A. Shaw, J. Halsall, and P. Hopkins. 2006. Mutations in RYR1 in malignant
1353 hyperthermia and central core disease. *Hum Mutat*. 27:977-989. doi: 10.1002/humu.20356.

1354 Sali, A., and T.L. Blundell. 1993. Comparative protein modelling by satisfaction of spatial restraints. *J Mol*
1355 *Biol*. 234:779-815. doi: 10.1006/jmbi.1993.1626.

1356 Samso, M. 2017. A guide to the 3D structure of the ryanodine receptor type 1 by cryoEM. *Protein Sci*.
1357 26:52-68. doi: 10.1002/pro.3052.

1358 Schneider, M.F., and B.J. Simon. 1988. Inactivation of calcium release from the sarcoplasmic reticulum in
1359 frog skeletal muscle. *J Physiol*. 405:727-745. doi: 10.1113/jphysiol.1988.sp017358.

1360 Sievers, F., A. Wilm, D. Dineen, T.J. Gibson, K. Karplus, W. Li, R. Lopez, H. McWilliam, M. Remmert, J.
1361 Soding, J.D. Thompson, and D.G. Higgins. 2011. Fast, scalable generation of high-quality protein
1362 multiple sequence alignments using Clustal Omega. *Mol Syst Biol*. 7:539. doi:
1363 10.1038/msb.2011.75.

1364 Sleiman, Y., A. Lacampagne, and A.C. Meli. 2021. "Ryanopathies" and RyR2 dysfunctions: can we further
1365 decipher them using in vitro human disease models? *Cell Death Dis*. 12:1041. doi:
1366 10.1038/s41419-021-04337-9.

1367 Steele, T.W.E., and M. Samso. 2019. The FKBP12 subunit modifies the long-range allosterism of the
1368 ryanodine receptor. *J Struct Biol*. 205:180-188. doi: 10.1016/j.jsb.2018.12.007.

1369 Stern, M.D. 1992. Theory of excitation-contraction coupling in cardiac muscle. *Biophys J*. 63:497-517.
1370 doi: 10.1016/S0006-3495(92)81615-6.

1371 Stern, M.D., G. Pizarro, and E. Rios. 1997. Local control model of excitation-contraction coupling in
1372 skeletal muscle. *J Gen Physiol*. 110:415-440. doi: 10.1085/jgp.110.4.415.

1373 Tencerova, B., A. Zahradnikova, J. Gaburjakova, and M. Gaburjakova. 2012. Luminal Ca2+ controls
1374 activation of the cardiac ryanodine receptor by ATP. *J Gen Physiol*. 140:93-108. doi:
1375 10.1085/jgp.201110708.

1376 Uehara, A., T. Murayama, M. Yasukochi, M. Fill, M. Horie, T. Okamoto, Y. Matsuura, K. Uehara, T.
1377 Fujimoto, T. Sakurai, and N. Kurebayashi. 2017. Extensive Ca2+ leak through K4750Q cardiac
1378 ryanodine receptors caused by cytosolic and luminal Ca2+ hypersensitivity. *J Gen Physiol*.
1379 149:199-218. doi: 10.1085/jgp.201611624.

1380 Wagenknecht, T., and M. Samso. 2002. Three-dimensional reconstruction of ryanodine receptors. *Front*
1381 *Biosci*. 7:d1464-1474. doi: 10.2741/A853.

1382 Wang, J., A. Jain, L.R. McDonald, C. Gambogi, A.L. Lee, and N.V. Dokholyan. 2020. Mapping allosteric
1383 communications within individual proteins. *Nat Commun*. 11:3862. doi: 10.1038/s41467-020-
1384 17618-2.

1385 Wei, R., X. Wang, Y. Zhang, S. Mukherjee, L. Zhang, Q. Chen, X. Huang, S. Jing, C. Liu, S. Li, G. Wang, Y. Xu,
1386 S. Zhu, A.J. Williams, F. Sun, and C.C. Yin. 2016. Structural insights into Ca(2+)-activated long-
1387 range allosteric channel gating of RyR1. *Cell Res*. 26:977-994. doi: 10.1038/cr.2016.99.

1388 Wilson, A.D., J. Hu, C. Sigalas, E. Venturi, H.H. Valdivia, C.R. Valdivia, M. Lei, M. Musgaard, and R.
1389 Sitsapesan. 2021. The V2475F CPVT1 mutation yields distinct RyR2 channel populations that
1390 differ in their responses to cytosolic Ca(2+) and Mg(2). *J Physiol*. 599:5179-5201. doi:
1391 10.1113/JP281707.

1392 Wilson, M.A., and A.T. Brunger. 2000. The 1.0 A crystal structure of Ca(2+)-bound calmodulin: an
1393 analysis of disorder and implications for functionally relevant plasticity. *J Mol Biol*. 301:1237-
1394 1256. doi: 10.1006/jmbi.2000.4029.

1395 Witherspoon, J.W., and K.G. Meilleur. 2016. Review of RyR1 pathway and associated pathomechanisms.
1396 *Acta Neuropathol Commun*. 4:121. doi: 10.1186/s40478-016-0392-6.

1397 Woll, K.A., O. Haji-Ghassemi, and F. Van Petegem. 2021. Pathological conformations of disease mutant
1398 Ryanodine Receptors revealed by cryo-EM. *Nat Commun*. 12:807. doi: 10.1038/s41467-021-
1399 21141-3.

1400 Xiong, H., X. Feng, L. Gao, L. Xu, D.A. Pasek, J.H. Seok, and G. Meissner. 1998. Identification of a two EF-
1401 hand Ca2+ binding domain in lobster skeletal muscle ryanodine receptor/Ca2+ release channel.
1402 *Biochemistry*. 37:4804-4814. doi:

1403 Xu, L., G. Mann, and G. Meissner. 1996. Regulation of cardiac Ca2+ release channel (ryanodine receptor)
1404 by Ca2+, H+, Mg2+, and adenine nucleotides under normal and simulated ischemic conditions.
1405 *Circ Res*. 79:1100-1109. doi:

1406 Zahradnik, I., S. Gyorke, and A. Zahradnikova. 2005. Calcium activation of ryanodine receptor channels--
1407 reconciling RyR gating models with tetrameric channel structure. *J Gen Physiol*. 126:515-527.
1408 doi:

1409 Zahradnikova, A., M. Dura, I. Gyorke, A.L. Escobar, I. Zahradnik, and S. Gyorke. 2003. Regulation of
1410 dynamic behavior of cardiac ryanodine receptor by Mg2+ under simulated physiological
1411 conditions. *Am J Physiol Cell Physiol*. 285:C1059-1070. doi:

1412 Zahradnikova, A., B. Iaparov, and I. Zahradnik. 2020. The problem of accuracy in single-channel open
1413 probability measurements. *Prog Biophys Mol Biol*. 157:94-106. doi:
1414 10.1016/j.pbiomolbio.2020.05.002.

1415 Zahradnikova, A., I. Valent, and I. Zahradnik. 2010. Frequency and release flux of calcium sparks in rat
1416 cardiac myocytes: a relation to RYR gating. *J Gen Physiol*. 136:101-116. doi:
1417 10.1085/jgp.200910380.

1418 Zheng, W., and H. Wen. 2020. Investigating dual Ca(2+) modulation of the ryanodine receptor 1 by
1419 molecular dynamics simulation. *Proteins*. 88:1528-1539. doi: 10.1002/prot.25971.

1420 Zhou, Y., W. Yang, M. Kirberger, H.W. Lee, G. Ayalasomayajula, and J.J. Yang. 2006. Prediction of EF-hand
1421 calcium-binding proteins and analysis of bacterial EF-hand proteins. *Proteins*. 65:643-655. doi:
1422 10.1002/prot.21139.

1423 Ziman, A.P., C.W. Ward, G.G. Rodney, W.J. Lederer, and R.J. Bloch. 2010. Quantitative measurement of
1424 Ca(2)(+) in the sarcoplasmic reticulum lumen of mammalian skeletal muscle. *Biophys J*. 99:2705-
1425 2714. doi: 10.1016/j.bpj.2010.08.032.

1426

Structure-based mechanism of RyR channel operation by calcium and magnesium ions

Alexandra Zahradníková[1]✉, Jana Pavelková[1], Miroslav Sabo[2], Sefer Baday[3], and Ivan Zahradník[1]✉

[1] Department of Cellular Cardiology, Institute of Experimental Endocrinology, Biomedical Research Center, Slovak Academy of Sciences, Bratislava, Slovakia. [2] Bioinformatics Laboratory, Biomedical Research Center, Slovak Academy of Sciences, Bratislava, Slovakia. [3] Applied Informatics Department, Informatics Institute, Istanbul Technical University, Istanbul, Türkiye.

Expanded View Figure EV1 – EV2

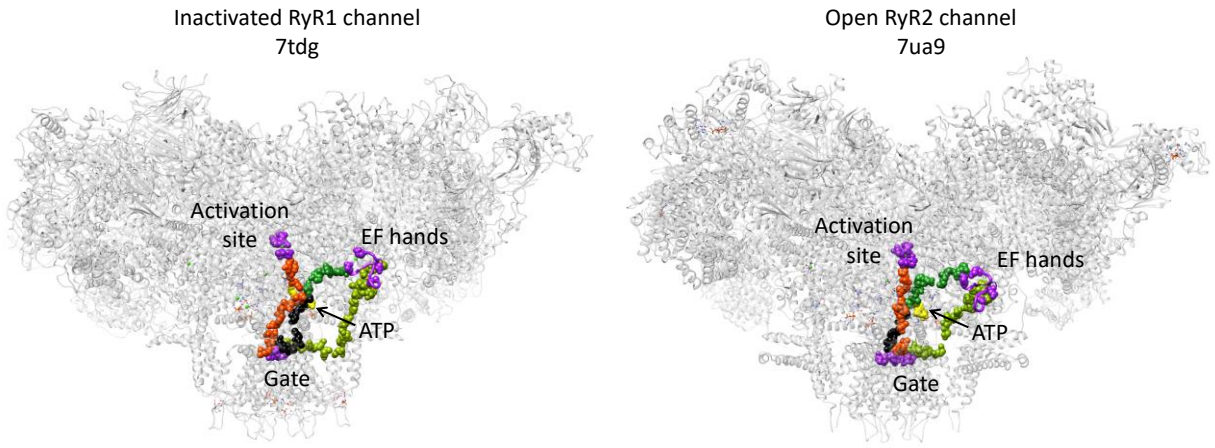

Figure EV1. Examples of the allosteric networks in RyR1 and RyR2. Allosteric and activation sites: purple. Activation pathways: red. Inhibition pathways: green. Common activation and inhibition pathways: black. ATP/ACP molecule: yellow.

Figure EV1 complements Figure 8.

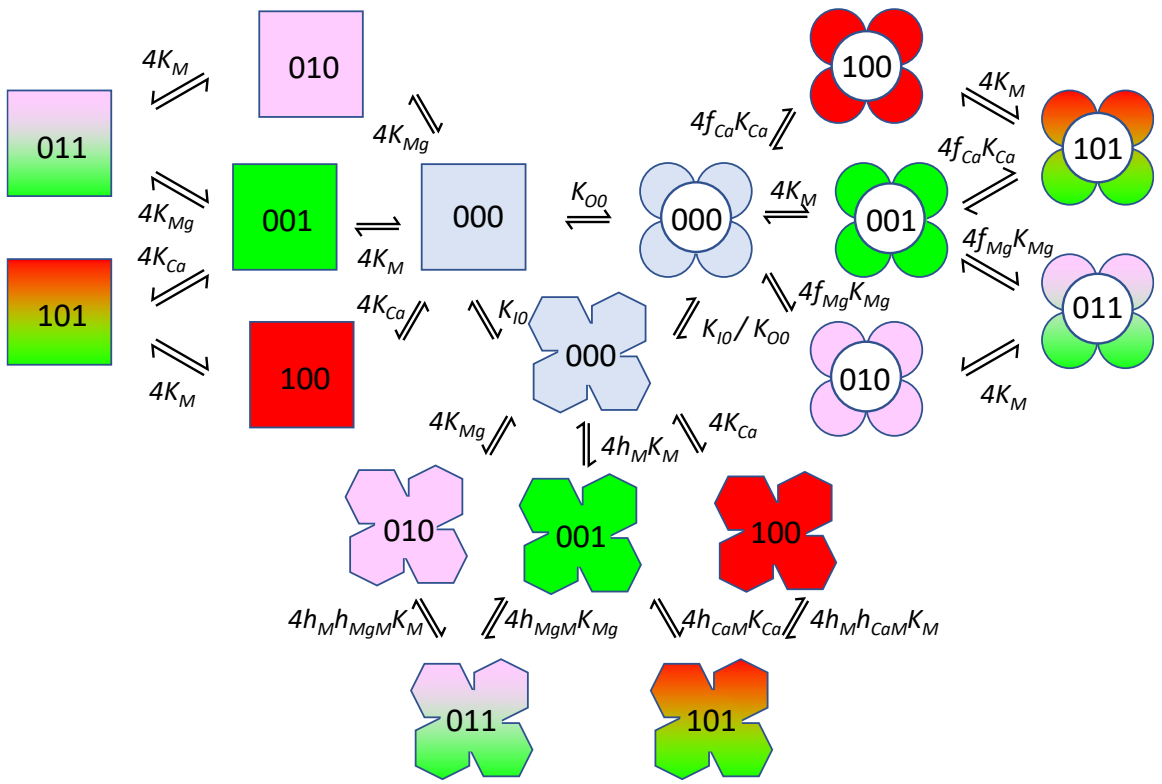

Figure EV2. Transitions between and within macrostates of the RyR tetramer. The overall representation of the model cannot be depicted on a two-dimensional plane, therefore the transitions between microstates are shown only for the binding of the first ion (Ca^{2+} or Mg^{2+}) to the activation site and the first divalent ion M^{2+} to the inhibition site. Other states and transitions can be constructed in the same way. The number of Ca^{2+} ions bound to the activation site is i = 0 to 4; the number of Mg^{2+} ions bound to the activation site is j = 0 to 4-i, and the number of M^{2+} ions bound to the inhibition site is k = 0 – 4. Squares: closed state; quatrefoils with a central opening: open state; angular quatrefoils: inactivated state. The channels with 1 Ca^{2+} bound to the activation site are shown in red; channels with 1 Mg^{2+} bound to the activation site are shown in pink; channels with 1 M^{2+} bound to the inhibition site are shown in purple. Channels with both the activation and the inhibition site occupied by one ion are shown in the red/green or pink/green gradient. The three digits inside the shapes denote respectively, from left to right, the number of Ca^{2+} ions at the activation site, the number of Mg2+ ions at the activation site, and the number of M^{2+} ions at the inhibition site. Note that the ion-binding dissociation constants are 4x larger than those in Figure 9 since in the ion-free tetramer, there are 4 possibilities to bind an ion to each of the binding sites, and in a tetramer with a single bound ion, there is one possibility to dissociate the ion. In addition, since all transitions are reversible, the product of each reaction cycle in the clockwise and anticlockwise directions is equal. Transitions between macrostates are shown only for the ligand-free channel but are present between all same-colored channels.

Figure EV1 complements Figure 9.